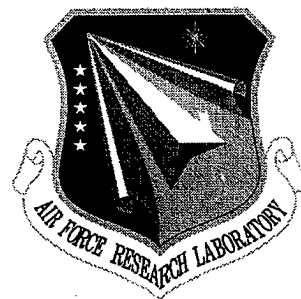AFRL-SN-RS-TR-1998-133
Final Technical Report
July 1998

PULSE GENERATION AND PROPAGATION IN OPTICAL FIBERS: EXPERIMENTS AND SIMULATION

Rensselaer Polytechnic Institute

Joseph W. Haus, Walter Kaechele, and Gary Shaulov

APPROVED FOR PUBLIC RELEASE; DISTRIBUTION UNLIMITED.

19980819 031

**AIR FORCE RESEARCH LABORATORY
SENSORS DIRECTORATE
ROME RESEARCH SITE
ROME, NEW YORK**

DTIC QUALITY INSPECTED 1

This report has been reviewed by the Air Force Research Laboratory, Information Directorate, Public Affairs Office (IFOIPA) and is releasable to the National Technical Information Service (NTIS). At NTIS it will be releasable to the general public, including foreign nations.
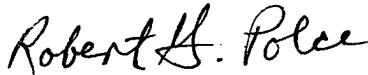
AFRL-IF-RS-TR-1998-133 has been reviewed and is approved for publication.

APPROVED: *[signature]*

JAMES P. THEIMER
Project Engineer

FOR THE DIRECTOR: *[signature]*

ROBERT G. POLCE, Acting Chief
Rome Operations Office
Sensors Directorate

REPORT DOCUMENTATION PAGE

1. AGENCY USE ONLY (Leave blank)	2. REPORT DATE	3. REPORT TYPE AND DATES COVERED
	July 1998	Final Jan 97 - Jan 98

4. TITLE AND SUBTITLE

PULSE GENERATION AND PROPAGATION IN OPTICAL FIBERS: EXPERIMENTS AND SIMULATION

6. AUTHOR(S)

Joseph W. Haus, Walter Kaechele, and Gary Shaulov

5. FUNDING NUMBERS

C - F30602-97-2-0069
PE - 62702F
PR - 4600
TA - P5
WU - PY

7. PERFORMING ORGANIZATION NAME(S) AND ADDRESS(ES)

Rensselaer Polytechnic Institute
110 Eighth Street
Troy NY 12180-3590

8. PERFORMING ORGANIZATION REPORT NUMBER

N/A

9. SPONSORING/MONITORING AGENCY NAME(S) AND ADDRESS(ES)

Air Force Research Laboratory/SNDR
25 Electronic Parkway
Rome NY 13441-4515

10. SPONSORING/MONITORING AGENCY REPORT NUMBER

AFRL-SN-RS-TR-1998-133

11. SUPPLEMENTARY NOTES

Air Force Research Laboratory Project Engineer: James Theimer/SNDR/(315) 330-4870

12a. DISTRIBUTION AVAILABILITY STATEMENT

Approved for public release; distribution unlimited.

12b. DISTRIBUTION CODE

13. ABSTRACT *(Maximum 200 words)*

Properties of active and passive mode-locked fiber lasers were examined. The experimental lasers displayed stable picosecond pulse generation and the noise in each mode-locked fiber laser was carefully characterized. The project included computational and analytical calculations and coordination of theoretical efforts with experimental efforts at the Photonics Center. Physical aspects of the cavity design were considered to help understand the operation of our fiber lasers.

14. SUBJECT TERMS

Fiber Lasers, Mode-Locked Lasers, Laser Noise, Laser Synchronization

15. NUMBER OF PAGES

60

16. PRICE CODE

17. SECURITY CLASSIFICATION OF REPORT	18. SECURITY CLASSIFICATION OF THIS PAGE	19. SECURITY CLASSIFICATION OF ABSTRACT	20. LIMITATION OF ABSTRACT
UNCLASSIFIED	UNCLASSIFIED	UNCLASSIFIED	UL

Table of Contents

List of Figures

1 Introduction

The primary goal of our investigation was the design and application of mode-locked fiber lasers and of photonic devices. The experiments were performed at the Photonics Center, where essential equipment was available. Government personnel and other university researchers formed a cohesive working group to successfully complete the project. Scientists involved in the project primarily includes Mike Hayduk and Jim Theimer from the Photonics Laboratory; and Ken Teegarden and Gary Wicks from the University of Rochester. Others at the Photonics Laboratory were very helpful of their time and resources.

The theoretical support was conducted parallel to the Rome experiments; it consisted of mathematical modeling and computational simulation techniques. Together the two efforts achieved a level of fundamental understanding that was important for future development and progress in this field. One impetus for the proposed problems are the future development of fiber-optic sources that can sample signals and serve as clock for A/D conversion of RF signals. We now have the experience and knowledge base to make contributions to this field.

Walt Kaechele developed experimental methods to measure and characterize the noise in model-locked lasers and analyzed to understand the dominant noise contributions in a laser design [1]. The stochastic theory of noise in mode-locked lasers has recently been examined for communications applications[2]. However, there is a need to adapt the analysis to mode-locked fiber lasers used at the Photonics Center.

Modelocked Erbium-doped fiber lasers have recently attracted attention primary due to their potential as compact sources of ultrafast ($< 1\ ps$) pulses in the wavelength regime of 1.55 μm [3]. There are several applications for compact ultrashort sources; fiber lasers are of interest for telecommunications or local area networks. Various fiber lasers designs have been demonstrated using passive modelocking techniques operating both in normal and anomalous dispersion regimes. The passive modelocked laser has been successfully operated by methods employing either a saturable absorber in the cavity or when the nonlinear properties of a fiber play the role of "artificial" saturable absorber. The latter include additive-pulse modelocking (APM) using, for example, nonlinear polarization rotation or a nonlinear loop mirror. Recently semiconductor saturable absorbers have been used to modelock linear fiber cavities [4, 5, 6], (usually it is semiconductor material in the form of bulk, multiple quantum well (MQW) or single quantum well - Saturable Bragg Reflector (SBR)). Bandgap engineering and semiconductor growth technology was used to fabricate saturable absorbers with accurate control of the device parameters such as absorption wavelength, saturation energy, and recovery time.

Recently ultrashort pulses generated both in solid-state and fiber lasers modelocked by a slow saturable absorber (i.e. recovery time is much longer than the final pulse width) were reported [5, 6, 7, 8]. Traditional modelocking schemes rely either on the fast saturable absorber or the interplay between a slow saturable absorber and gain saturation, as in the case with dye lasers. By contrast, in a mode locked laser stabilized with a slow absorber the net gain window does not close immediately after passage of the pulse. This is possible in the soliton regime because the nonlinear effects due to self-phase modulation are in balance with the linear effects due to the negative group

1

velocity dispersion.

In this report we present experimental, theoretical and numerical studies of a fiber laser modelocked by multiple quantum well (MQW) slow saturable absorber. A compact, polarization insensitive, modelocked fiber laser using a GaInAs/AlInAs MQW as the saturable absorber mirror element was recently reported [7, 8]. Recovery time of saturable absorbers was varied from 500 ps to 2 ns. Stable pulses are generated whose pulse width ranges from 1 to 50 ps depending on physical properties of the saturable absorber. Parameters for this laser were used in numerical simulations and results were compared with the experimental data.

2 Passive Mode-locked Lasers: Theory

The theory of fiber laser modelocking is based on an average equation [9, 10] derived under the condition that nonlinear changes to the intracavity pulse must be small per round-trip and soliton perturbation theory assumed that pulse dynamics deviate by small factor from soliton solution. In many modelocked fiber lasers these conditions do not necessarily hold, nevertheless, the theory can be modified to accommodate this new situation. The average equation belongs to the class of generalized complex Ginzburg-Landau (CGL) equations and has a form

$$\frac{\partial A}{\partial z} = i\left(D\frac{\partial^2}{\partial t^2} + \delta|A|^2\right)A + \left(g - l_0 + D_{g,f}\frac{\partial^2}{\partial t^2} - Q(z,t)\right)A. \tag{1}$$

Here A is the optical field complex amplitude, t is a reduced physical time and z is the distance divided by the cavity round-trip length L_c. D is a cavity dispersion, δ is Kerr nonlinearity coefficient, $D_{g,f}$ - gain and intracavity filter dispersion, l_0 and g are linear losses and gain per round-trip, respectively. Parameters D, $D_{g,f}$ and δ_3 are defined as:

$$D = -\frac{\beta_2 L_c}{2}, \quad D_{g,f} = \frac{g}{\Omega_g{}^2} + \frac{1}{\Omega_f{}^2}, \quad \delta_3 = \frac{2\pi n_2}{\lambda_0 A_{eff}}L_c,$$

we also relate the bandwidth frequencies to their wavelength bandwidth by the relations $\Omega_f = 2\pi c\Delta\lambda_f/\lambda_0{}^2$ and $\Omega_g = 2\pi c\Delta\lambda_g/\lambda_0{}^2$, where β_2 is a group velocity dispersion (GVD), n_2 is a nonlinear refractive index, λ_0 is the center wavelength of the pulse, A_{eff} is the effective fiber core area, and $\Omega_{g(f)}$ - gain(filter) bandwidth. The function $Q(z,t)$ in Eqn.(1) is the response of the saturable absorber which can be modeled by two-level system rate equation

$$\frac{\partial Q}{\partial t} = -\frac{Q - Q_0}{T_A} - \frac{|A|^2}{E_A}Q, \tag{2}$$

where Q_0 is an absorption coefficient, T_A and $E_A = P_A\,T_A$ are saturable absorber relaxation time, saturation energy and power, respectively.

2.1 Soliton Regime

No analytic solutions to the full complex Ginzburg-Landau equation, Eq.(1), are known. Without the dissipative terms due to gain and loss, Eq.(1) reduces to the nonlinear

2

Schrödinger (NLS) equation

$$\frac{\partial A}{\partial z} = i\left(D\frac{\partial^2}{\partial t^2} + \delta|A|^2\right)A + P[A, A^*].$$ (3)

The terms $P[A, A^*]$ are perturbations to the NLS equation, which has the following fundamental solution in case of negative dispersion

$$A_s(z,t) = A_0 \text{sech}[x(z,t)]\exp(i\theta(z,t)),$$ (4)

where

$$x(z,t) = \frac{1}{\tau}(t + 2Dp_0z - t_0),$$ (5)

is the retarded time normalised to the pulse width τ, and the total phase is given by

$$\theta(z,t) = -p_0t - D(\frac{1}{\tau^2} - p_0^2)z + \theta_0.$$ (6)

and p_0 is a frequency offset, t_0 - timing shift and θ_0 - initial phase. The energy contained in the soliton is related with its amplitude via

$$W = \int_{-\infty}^{\infty} |A|^2 dt = 2A_0^2\tau;$$ (7)

and is a integral of motion. Balance between dispersion and nonlinearity leads to relation between soliton amplitude and width, so-called soliton area theorem:

$$A_0^2\tau^2 = \frac{2|D|}{\delta}.$$ (8)

In the case when Eq.(3) is valid, i.e. parameters $D_{g,f}, Q_0, l_0, g$ are much smaller that D, δ, we can use soliton perturbation theory and look for a solution of Eq.(1) in the form of sech-shape pulse

$$A = A_0 \text{sech}\left(\frac{t}{\tau}\right).$$ (9)

First we can find exact solution of Eq.(2)

$$Q(z,t) = \frac{Q_0}{T_A}\int_{-\infty}^{t}\exp\left(-\frac{t-t'}{T_A} - \frac{1}{E_A}\int_{t'}^{t}|A|^2 dt''\right)dt'$$ (10)

In the case when pulse has a sech shape we can rewrite Eq.(10) as:

$$Q = Q_0\epsilon\int_{-\infty}^{x}\exp\left(-\epsilon(x-x') - \frac{W}{2E_A}(\tanh(x) - \tanh(x'))\right)dx';$$ (11)

with $\epsilon = \frac{\tau}{T_A}$ and $x = \frac{t}{\tau}$.

Fig. (1) shows the absorbance response Q for sech shape pulse and for different ratios between pulse and absorber relaxation time. Saturable absorber depending on its relaxation time T_A compared with the pulse width τ can work in two regimes: as a

3
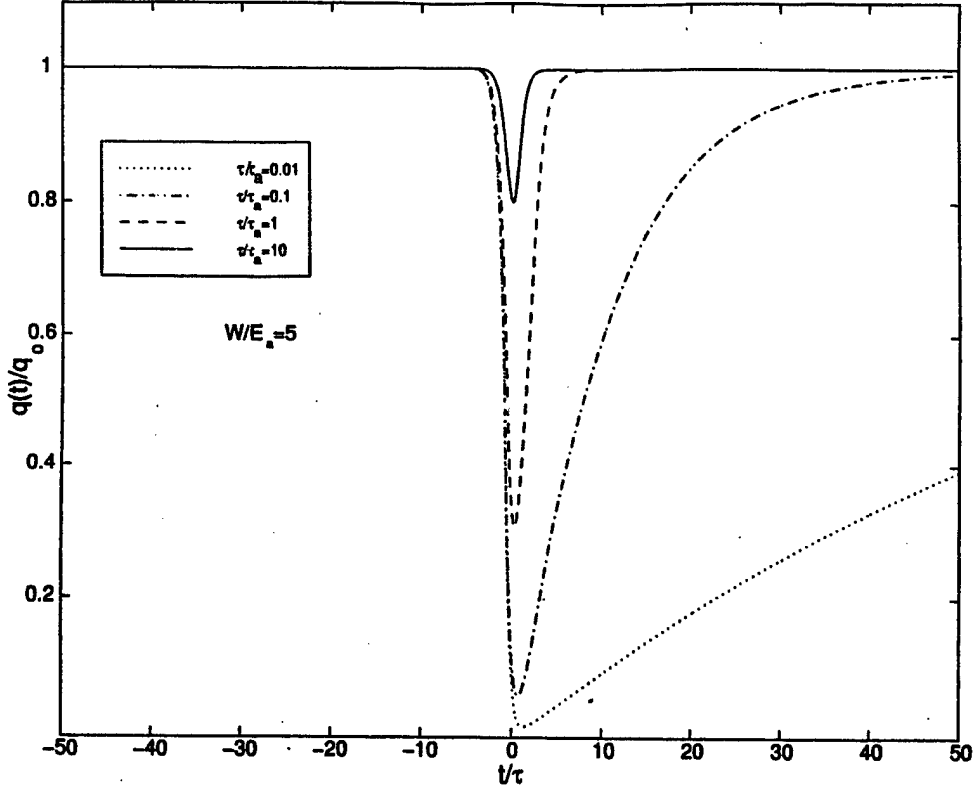
Figure 1: Response of the saturable absorber excited by a sech-pulse shape. Different relaxation times are used, as indicated.

fast saturable absorber (FSA) when $T_A << \tau$ or a slow saturable absorber (SSA) when $T_A >> \tau$.

For the case of a fast absorber, $\epsilon \to \infty$, we obtain

$$Q(z,t) = \frac{Q_0}{1 + \frac{|A|^2}{P_A}};$$ (12)

and further if we assume that pulse power less than saturation power, we can expand the denominator in Eq. (12)

$$Q(z,t) = Q_0 \left(1 - \frac{|A|^2}{P_A} + \frac{|A|^4}{P_A^2} \right).$$ (13)

Substituting Eq.(10) in our master Eq.(1) we obtain the quintic CLG equation

$$\frac{\partial A}{\partial z} = i \left(D\frac{\partial^2}{\partial t^2} + \delta|A|^2 \right) A + \left(g - l + D_{g,f}\frac{\partial^2}{\partial t^2} + \gamma_3|A|^2 - \gamma_5|A|^4 \right) A,$$ (14)

where $l = l_0 + Q_0$, $\gamma_3 = \frac{Q_0}{P_A}$, $\gamma_5 = \frac{Q_0}{P_A^2}$.

In the opposite limit of very slow relaxation time, i.e. $\epsilon \to 0$ the absorber response can be given by

$$Q(z,t) = Q_0 \exp\left(-\frac{1}{E_A} \int_{-\infty}^{t} |A|^2 dt' \right) = Q_0 \exp\left(-\frac{W}{2E_A}[1 + \tanh(x)] \right).$$ (15)

4

Now using soliton perturbation theory we obtain the evolution equation for pulse energy:

$$\frac{\partial W}{\partial z} = 2\left[(g - l_0) - \frac{1}{3}\frac{D_{f,g}}{\tau^2} - \bar{Q}(\tau)\right]W, \tag{16}$$

where

$$\bar{Q}(\tau; T_A, P_A, D, \delta) = \frac{\int_{-\infty}^{\infty} Q|A|^2 dt}{\int_{-\infty}^{\infty} |A|^2 dt}; \tag{17}$$

besides the free parameter τ, also depends on relaxation time, saturation power P_A, and through soliton-area theorem on dispersion D and Kerr coefficient δ.

This equation imply that laser reaches steady state when the gain equals the losses experienced by the solitary pulse

$$g = l_0 + \frac{1}{3}\frac{D_{f,g}}{\tau^2} + \bar{Q}(\tau) \equiv l_{eff}. \tag{18}$$
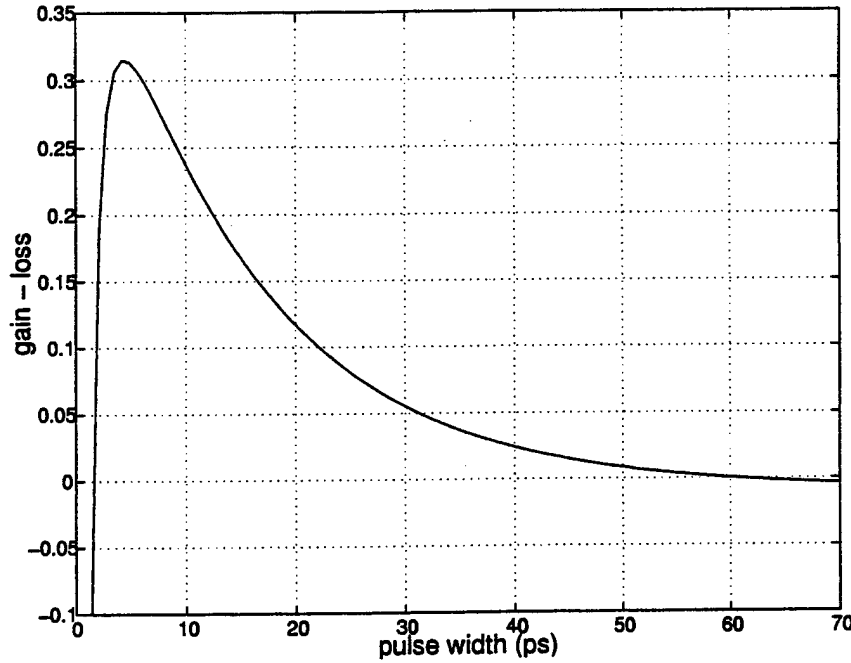
Figure 2: Solutions for the steady-state energy. Assuming a sech-pulse shape.

The analysis revealed that this energy balance equation can have two, one or zero steady-state pulse solutions, depending on choice of the laser parameters such as gain, absorption coefficient (depending on a number of MWQ), filter bandwidth, etc. $g - l_{eff} < 0$ for shorter and longer pulses (lower and higher energies) and $g - l_{eff} > 0$ for intermediate pulse widths. In the case of two solutions we can expect that shorter pulses are stable and the broader ones unstable (since shorter τ increase(decrease) then $g - l_{eff}$ increase(decrease), whereas broader τ increase(decrease) then $g - l_{eff}$ decrease(increase)). Fig. (2) shows for following parameters for our laser: $Q_0 = 0.25$, $g - l = 0.005$, $T_A = 700$ ps, $I_s = 12$ kW/cm^2, $\lambda_f = 1$ nm. For this case $D_{f,g} = 1.6$ ps^2. The soliton shaping is determined from the fiber dispersion parameter $\beta_2 = -10$ps^2/Km and the

fiber nonlinearity. Later we will include the dispersive nonlinearity from the saturable absorber. Taking these parameters we have two steady state solutions with pulse widths $\tau = 1.5$ ps, and $\tau = 60$ ps. The shorter pulse width is always stable and the longer one is unstable. This result is obtained from a local stability analysis of the evolution equation.

Fig. (3) has the numerically computed pulse evolution for slow saturable absorber and Fig. (4) compare the initial pulse with the steady-state result. For the initial pulse we use an unchirped soliton with parameters chosen near that determined by energy balance. After steady-state is reached the pulse's temporal and spectral profiles have correspondingly changed. The parameters used in these figures are: $Q_0 = 0.003$, $l = 0.5$, $g = 0.495$, and $T_A = 500$ ps. All other parameters are chosen as in Fig. (2). The initial FWHM pulse width is 5 ps, whereas in steady state the final value FWHM is about 10 ps. The initial pulse is unchirped, while the final one is chirped. The chirp is most easily determined from Fig. (4), where the FWHM spectral widths are almost the same between the initial and steady-state spectra.
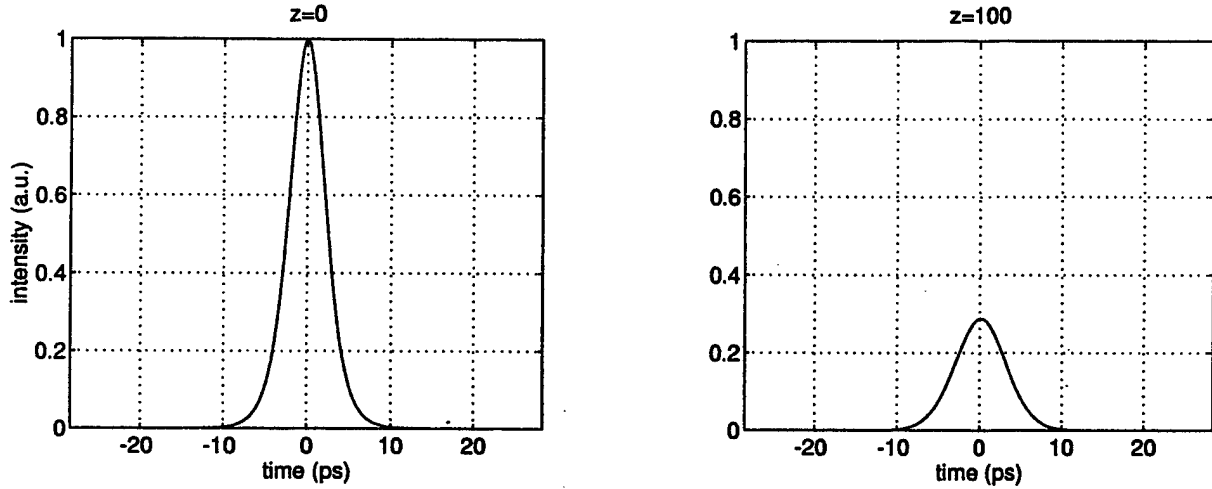
Figure 3: Steady-state pulse shape from the model.

For the case of very slow saturable absorber we can use Eq. (15) to find analytical form for energy balance equation:

$$g = l_0 + \frac{1}{3}\frac{D_{f,g}}{\tau^2} + Q_0 \frac{E_A}{W}\left(1 - e^{-W/E_A}\right) \equiv l_{eff} \tag{19}$$

For fast saturable absorber we have:

$$g = l + \frac{D_{f,g} - 2\gamma_3\kappa}{3\tau^2} + \frac{8\gamma_5\kappa^2}{15\tau^4} \equiv l_{eff} \tag{20}$$

The last equation is quadratic equation for τ^2 and we can find explicit dependence of steady-state pulse width on the laser parameters. Fig. (5) shows the pulse width versus parameters $I_s, \beta_2, Q_0, \Omega_f$ calculated from Eq. (20) and numerically computed from
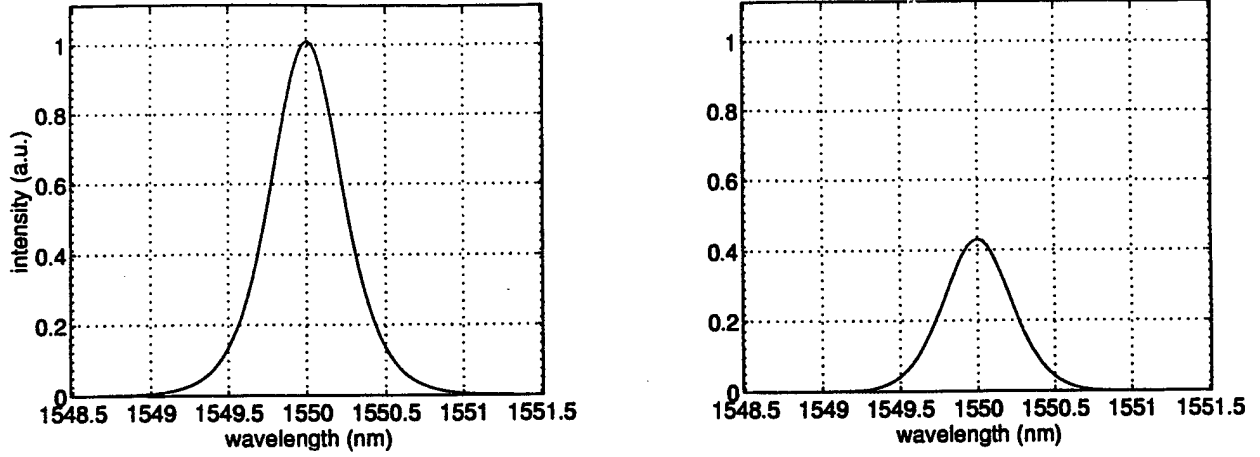
Figure 4: Spectrum of the pulse.

Eq. (1). The basic parameters were chosen close to the experimental values with a wide-band reflective mirror at one end of the cavity, $Q_0 = 0.003$, $l - g = 0.005$, $T_A = 700$ ps, $I_s = 12$ kW/cm^2, $\Delta\lambda_g = 30$ nm. In this case $D_{g,f} = 1.6 \times 10^{-3}$ ps^2. From this basic parameter set a single variable was chosen to vary; the four figures have the following parameter dependences 5(a) $\tau = \tau(I_s)$, 5(b) $\tau = \tau(Q_0)$, 5(c) $\tau = \tau(\beta_2)$, and 5(d) $\tau = \tau(\Delta_f)$.

The results of the numerical computations are compared against the results of soliton perturbation theory. There is generally a good agreement between the two, except for the case of small filter bandwidths Ω_f and large absorption coefficients Q_0. In these regions the soliton perturbation theory is no longer valid. Moreover, the analysis of the energy balance equation gives additional restrictions on relations between pulse parameters to steady-state solution to exist:

$$\frac{D_{g,f}}{D} \frac{\delta}{\gamma_3} > \frac{1}{4} \tag{21}$$

$$\frac{5}{24} \frac{Q_0}{l-g} \left(1 - \frac{D_{g,f}\delta}{4D\gamma_3}\right) \geq 1 \tag{22}$$

Equality in second equation corresponds to the case when there is only one solution.

When we account for the third-order dispersion (TOD) of the fiber, a new term is added to Eq. (1) the term $D_3\partial^3 A/\partial t^3$ where $D_3 = \beta_3 L_c/3!$. In this case the balance equation, Eq.(20) is also modified

$$\frac{D_{g,f}}{3\tau^2} \rightarrow \frac{D_{g,f}}{3\tau^2}\left(1 + \frac{2B^2}{5\tau^2}\right)$$

where $B = \frac{D}{6D_3}$. TOD can cause timing shifts and an asymmetry develops in the pulse

7
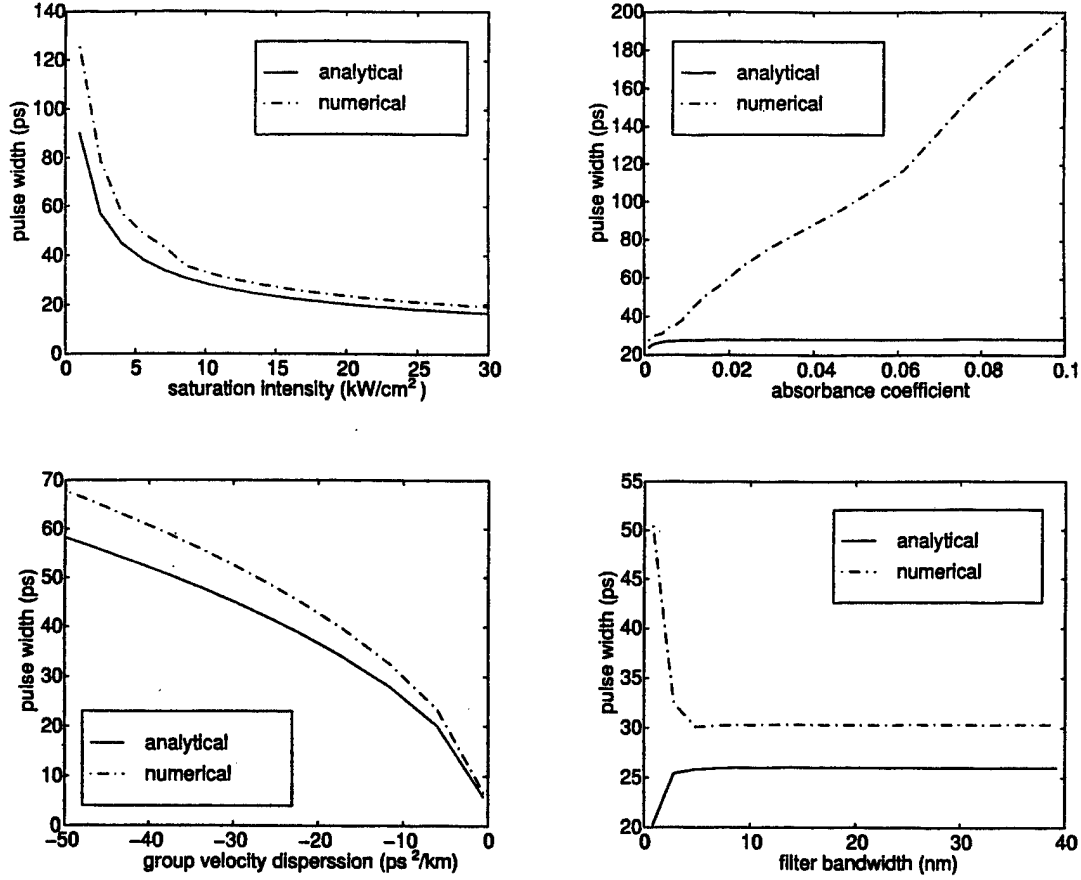
Figure 5: Predictions of the steady-state pulse width from numerical simulations and from soliton perturbation theory.

shape, but since $\beta_3 = 0.1\ ps^3/km$ for standard fiber and $B = 0.1\ ps^{-1}$, we found that the TOD effect can be neglected for pulses 1 ps and broader.

Next we also took in account that in the case of semiconductor absorbers the free carriers generated in the material contribute to the refractive index. Because the saturation of the absorption and the refractive index change are related to the excited carrier density, we assume that they proportional to each other as in semiconductor lasers. The refractive index can be implemented to Eq. (1) by a complex saturable absorption

$$Q(z,t) \rightarrow Q(z,t)(1+i\phi) \qquad (23)$$

By numerical simulations (taking ϕ in range from -10 to 10) we determined that this contribution causes an additional frequency shift, which is analogous to Raman self-frequency shift in fibers.

We observed that a pulse experiences a timing shift due to the asymmetric response of slow absorber (see Fig. (6)). For this case we used the parameters: $Q_0 = 0.03, \phi = 10, l = 0.5,\ g = 0.495,\ T_A = 500\ ps,\ I_s = 12\ kW/cm^2, and\ \Delta\lambda_g = 30\ nm$. The initial pulse has a FWHM of 10 ps and the asymmetric final pulse has a FWHM of about 8 ps. The spectrum develops considerable asymmetry, as well, and the peak shifts to longer wavelengths. For $\phi = 5$, the asymmetry is slight, but there is a measurable spectral shift.

8
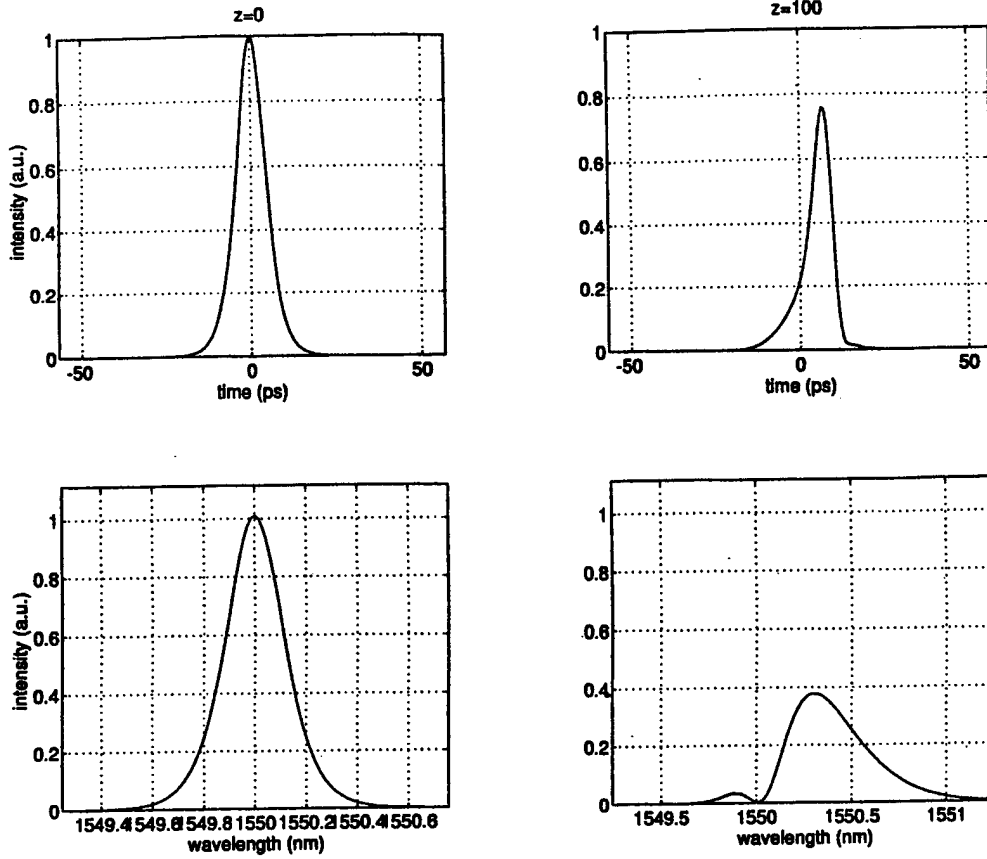
Figure 6: Effect of complex nonlinearity for slow saturable absorber model.

2.2 Non-soliton Regime

We also considered the case when laser parameters lie outside the regime where soliton perturbation theory would be valid, i.e. when dissipative part of Eq.(1) dominates over conservative (solitonic) part. Eq.(1) in the case of fast saturable absorber can be rescaled as a complex amplitude version of the nonlinear diffusion equation with a perturbation that has the solitonic part

$$\frac{\partial A}{\partial z} = \left(D_{g,f} \frac{\partial^2}{\partial t^2} + g - l + \gamma_3 |A|^2 - \gamma_5 |A|^4 \right) A + P[A, A^*] \tag{24}$$

Short cavity length, high doped fiber gain and high absorption in the case of MQW saturable absorber make fiber laser operate far from soliton regime. To the best of our knowledge Eq. (1) in this non-soliton limit has not yet been studied. Taking for example parameters of fiber laser modelocked by MWQ saturable absorber reported by Walt Kaechele [8] $L_c = 10\ m$, $\beta_2 = -10\ ps^2/km$, $Q_0 = 0.2$, $\Delta\lambda_f = 1\ nm$ we can see that $D = 0.05\ ps^2$, $D_{g,f} = 1.62\ ps^2$, $\delta = 2.6 \times 10^{-4}\ W^{-1}$ and $\gamma_3 = 1.5 \times 10^{-2}\ W^{-1}$, i.e. $D/D_{g,f} = 3.09 \times 10^{-2}$ and $\delta_3/\gamma_3 = 1.73 \times 10^{-2}$. can Then we can rescale Eq.(1)

$$\psi_Z = (1 + i\mu)\psi_{TT} - \alpha\psi + (1 + i\nu)|\psi|^2\psi - |\psi|^4\psi \tag{25}$$

where $\psi = \sqrt{1/P_A}\ A$, $Z = Q_0 z$, $T = \sqrt{Q_0/D_{g,f}}\ t$, $\mu = D/D_{g,f} \ll 1$ and $\nu = \delta_3/\gamma \ll 1$ and

$$\alpha = \frac{l - g}{Q_0}. \tag{26}$$

9

since μ and ν are very small parameters, we can neglect them in Eq.(25) and consider the unperturbed amplitude equation with real coefficients

$$\psi_Z = \psi_{TT} - \alpha\psi + |\psi|^2\psi - |\psi|^4\psi \qquad (27)$$

Such a class of amplitude equations was studied extensively due to their physical importance in optics [11], hydrodynamics [12], and pattern formation [13, 14].

Eq. (27) can be derived from a variational principle, in which the free energy density is given by

$$\mathcal{F} = \mathcal{T} - \mathcal{U} = |\psi_t|^2 + \alpha|\psi|^2 - \frac{1}{2}|\psi|^4 + \frac{1}{3}|\psi|^6; \qquad (28)$$

$\mathcal{T} = |\psi_t|^2$ is the kinetic energy density and $\mathcal{U}$ is the potential energy density. The function

$$F = \int \mathcal{F}dt, \qquad (29)$$

is a Lyapunov functional and stable stationary states are minima of F. The potential density function $\mathcal{U}$ in Fig. (7) has two maxima for a selection of values of the parameter α. The two maxima are equal for the value $\alpha = 3/16$.
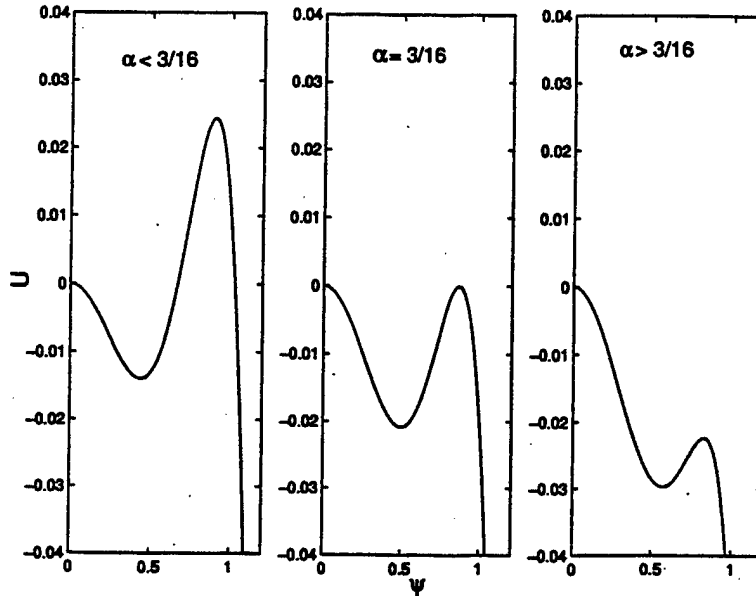
Figure 7: Potential function for two values of α.

By considering stationary solutions of the differential equation, we can derive traveling wave solutions of the form $\psi(z,t) = \psi(t - cz) = \psi(\tau)$, where c is the velocity. When this ansatz is put into Eq. (27), we have a second-order ordinary differential equation for a complex field and c appears as a damping coefficient. The ordinary differential equation is reduced to a set of dynamical equations by using the following substitution

$$\psi = v(\tau)e^{i\phi(\tau)}$$
$$u = v_\tau/v$$
$$\Omega = \phi_\tau. \qquad (30)$$

The resulting equations are

$$v_\tau = vu$$
$$u_\tau = -u^2 - cu + \Omega^2 + \alpha - v^2 + v^4$$
$$\Omega_\tau = -\Omega(2u + c). \tag{31}$$

There is a stationary solution in the invariant plane $\Omega = 0$, which has the fixed points
 The orbits, both homoclinic and heteroclinic determine the shape of the solutions. The fixed points of the dynamical equations and orbits are shown in Fig. (8). Points I and II have coordinates

$$v_0^{\pm} = \sqrt{\frac{1 \pm \sqrt{1 - 4\alpha}}{2}},$$
$$u = 0. \tag{32}$$

The coordinates of points III and IV are

$$v = 0,$$
$$u_0^{\pm} = -\frac{c}{2} \pm \sqrt{\left(\frac{c}{2}\right)^2 + \alpha}. \tag{33}$$
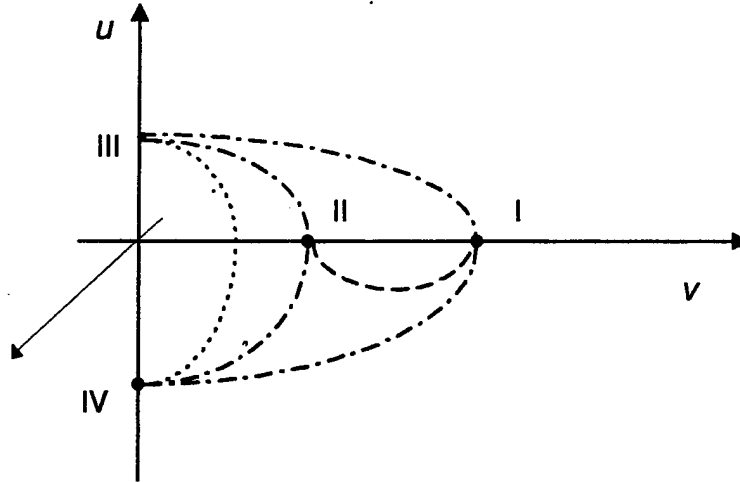
Figure 8: The invariant plane of the dynamical system. There are four fixed points.

Parameterized heteroclinic and homoclinic orbits determine the shape of the traveling wave solutions. Linear stability analysis reveals that fixed points I, III and IV are always saddle points and fixed point II is either a stable node $(c > 0)$, an unstable node $(c < 0)$ or an elliptic point $(c = 0)$.
 The heteroclinic orbits III→I or I→ IV describe front propagation. The solution is

$$\psi = \frac{v_0^+}{\sqrt{(1 + e^{-2a\tau})}}. \tag{34}$$

11

with $a = -(1+\sqrt{1-4\alpha})/2\sqrt{3}$ and the front velocity $c = (2\sqrt{1-4\alpha}-1)/\sqrt{3}$ ($\alpha < 1/4$). This solution is stable and its development from the partial differential equation, Eq. (27) is given in Fig. (9). The velocity of the front propagates with velocity c.
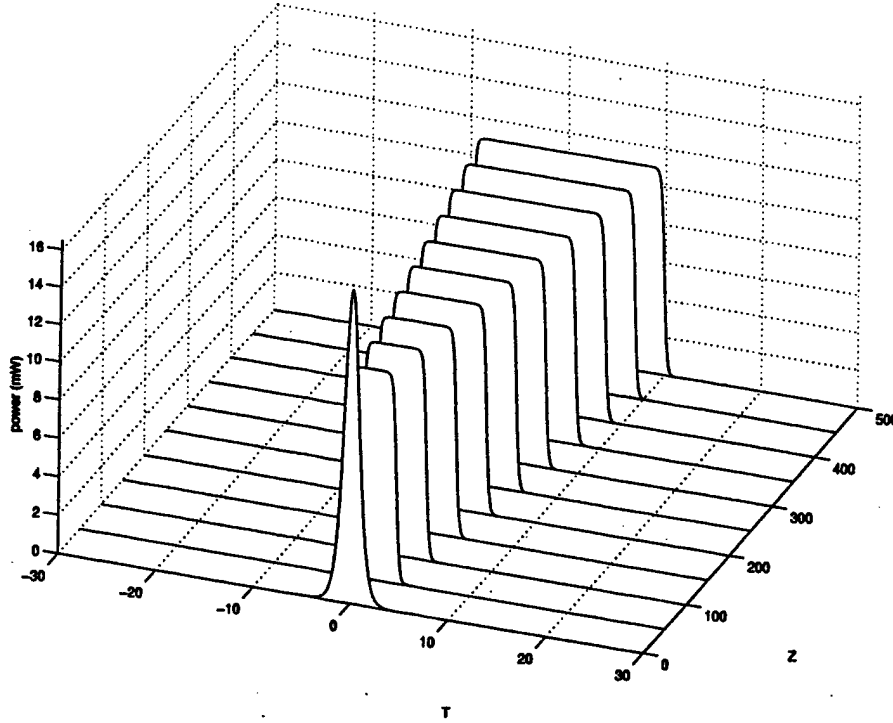
Figure 9: The evolution of an initial pulse according to Eq. (27). The form of the front and its velocity are accurately given from our analysis.

Orbits III to IV form pulse solutions when $c = 0$ and $\alpha < 3/16$. An example is shown in Fig. (10). The analytic form of the solution is

$$\psi = \sqrt{\frac{4\alpha}{1 + \sqrt{1 - 16\alpha/3}\cosh(\sqrt{4\alpha}\tau)}}e^{i\phi_0}. \tag{35}$$

We have identified all parameter ranges for α that are distinguished by different behavior and grey pulse solutions are found as well[15]. Pulse solutions are generally unstable, but may be stabilized by perturbations (μ and ν) that are sufficiently large, especially near the point $\alpha = 3/16$. At this time we have not analyzed how large the perturbations need to be that stabilize the pulse solutions; this is an issue that requires more research.

We suspect from the given design parameters of the fiber lasers used by our group, that the laser operates far from the soliton regime. For example, putting in the actual value of the absorption produces a value for $Q_0 = 0.3$, which as demonstrated in Fig. (5)(b) lies far outside the valid soliton perturbation regime. The pulse widths we find in the model, and the amount of chirp on the pulse, are in line with the experimental observations. However, the details of the lasers require more effort before we can conclusively declare that an explanation of the operating characteristics has been achieved.

12
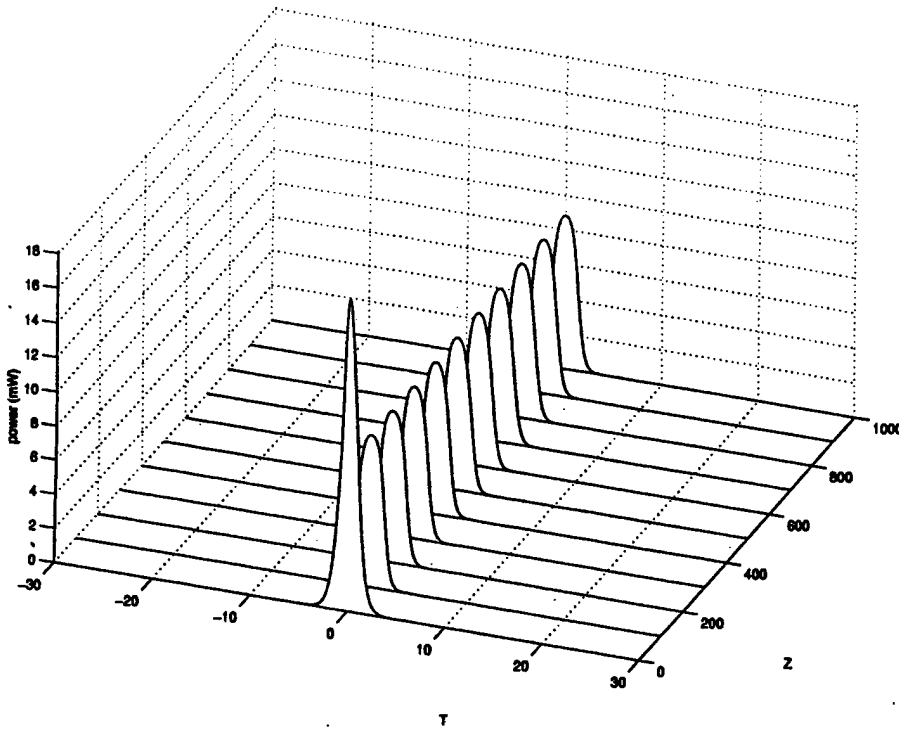
Figure 10: The pulse solution for $\alpha = 3/16$. At this point the front velocities are zero.

3 Mode-locked Lasers: Experiment

3.1 Actively Mode-Locked Erbium Fiber Ring Laser

An active mode-locked fiber laser was built by Walt Kaechele from the design of Harvey and Mollenauer. The acousto-optic modulator used in the laser design is particularly useful since it provides a completely integrated package without resorting to bulk optical components. The synchronization of the pulse train to an electrical drive allows the laser to be referenced to an external clock. This has particular advantages when the laser pulse train must be modulated by an electrical signal as is the case with digital communications.

Active mode-locking of erbium doped fiber lasers has been an area of intense interest since 1989 when it was realized that picosecond pulses could be obtained[16]. Operating as an actively mode-locked laser, the laser generated 50 ps pulses with sufficient bandwidth to support 2 ps pulses at a repetition rate of 90 MHz. The addition of 2 km of standard telecommunications fiber allowed the pulses to access the additional soliton pulse shaping mechanisms which occur in the anomalous dispersion regime reducing the pulse widths to 4 ps. Subsequent improvements in cavity design eliminated the need for these long cavities as soliton pulse-shaping in an actively mode-locked laser produced pulse widths below 2 ps in a harmonically mode-locked laser operating at 420 MHz[17]. The laser had a Fabry-Perot cavity with only ten meters of fiber which resulted in a cavity mode spacing of approximately 10 MHz. This laser was tunable over the entire erbium gain bandwidth from 1.521 - 1.58 μm, a property of erbium lasers which makes them attractive for a number of applications.

13

Following these initial experiments the performance of actively mode-locked fiber lasers has continued to improve. Erbium doped fiber lasers routinely provide transform limited picosecond pulses with repetition rates in the gigahertz range.[18] Stabilization techniques have reduced environmental fluctuations and thereby allowed extended operation with stable, equal amplitude pulse trains. Phase locking techniques to lock the pulse phase to a stable external source have been developed.[19] The inclusion of a pulse-rate étalon in a ring cavity stabilized a harmonically mode-locked laser when the free-spectral range of the cavity matched the operating repetition rate.[20] More recently, polarization preserving components have been added to eliminate the polarization mode dispersion which occurs in standard fiber lasers. This laser was capable of producing 6 ps pulses at repetition rates up to 40 GHz while being tunable over 50 nm of the erbium gain bandwidth[21].

Traditional operation of these lasers at harmonics of the cavity frequency has been well documented and characterized. If the drive signal to the modulator falls on specific frequencies between the cavity harmonics, it is possible to induce the laser to pulse at much higher repetition rates in a state known as rational harmonic mode-locking. By exploiting this method very high repetition rates are possible and have been demonstrated as high as 200 GHz.[22] The mechanisms of this method are limited by the available gain and relative linewidths of the axial modes as will be shown later. This method has renewed interest in the mode-locking mechanisms and potential applications of actively mode-locked fiber ring lasers.

The development and characterization of an actively mode-locked fiber ring laser and its operation in a number of frequency regimes ranging from megahertz to gigahertz is described in the following sections. This laser also serves as the source or master signal for the synchronization experiments described later. Characteristics of this laser which are considered include the pulse width, spectrum, energy and noise. Also we examined the rational harmonic mode-locking technique, a novel method enabling very high repetition rates to be obtained at relatively low drive frequencies, as a means of extending the laser capabilities.

3.1.1 Laser Configuration

This laser was based on the traditional design of actively mode-locked fiber ring lasers employing a fiber pigtailed Mach-Zehnder modulator.[18, 20, 23] The essential features of these lasers are an isolator, output coupler and modulator. Since the modulator is a polarization sensitive element, at least one polarization controller is required in the cavity to account for the birefringence of the cavity. The layout for this laser is shown in Fig. (11).

Four meters of erbium fiber provided by Mike Dennis and Irl Duling of the Naval Research Laboratory acted as the gain medium and was specifically designed to be compatible with standard monomode fiber, such as the industry standard Corning SMF-28. This simplified the splicing of this fiber length to the wavelength division multiplexer (WDM) as there was no significant difference in core diameters. The characteristic values provided with the fiber were listed as ~1.0 db/mW for the absorption with a dispersion of 11±3 ps/nm/km. The erbium was pumped by an SDL master oscillator/power amplifier
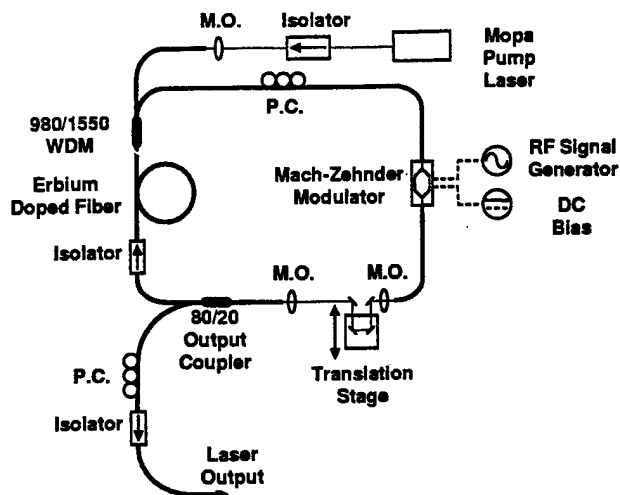
Figure 11: Schematic of the actively mode-locked ring laser.

(MOPA) diode laser which provided approximately 950 mW of power at a wavelength of 990 nm slightly off from the peak absorption value of 980 nm. The MOPA emits light in a diffraction limited TEM_{00} mode required for efficient coupling to single mode fiber. The pump light was focused onto a flat cleaved strand of Corning Flexcor 1060 fiber which is single mode at 990 nm. The fiber is single mode at the pump wavelength to prevent higher order transverse modes which could reduce efficiency by producing an intensity profile within the erbium fiber which is not Gaussian. Once optimized the pump delivered about 400 mW of power into the fiber core. Approximately 17 mW of pump light was measured coming out of the erbium fiber giving an absorption of 13.5 dB or 3.37 dB/m.

The primary component of the laser, except for the erbium doped fiber, was the lithium niobate Mach-Zehnder modulator. The modulator is designed to operate near 1550 nm, it has an operating bandwidth of 12 GHz with an insertion loss of 3.2 dB. A DC bias on the modulator allows the transmittance to be varied. The modulator exhibited an incredibly high extinction ratio in excess of 60 dB. The operation of the modulator requires only a single polarization. The input polarization crosstalk was given as 35.9 dB with an output polarization crosstalk of 41.6 dB. The highly polarization selective nature of the modulator allowed it to act as a fast saturable absorber permitting nonlinear pulse shaping to further reduce pulse widths. The free space delay line allowed fine adjustments to be made to the round trip time.

Additional lengths of fiber could be added to the cavity to provide a coarse adjustment to the cavity length to enable operation at a specific frequency with fine adjustments provided via the delay line. At low repetition rates additional fiber also allowed the nonlinear shaping mechanisms of APM to take place significantly reducing the pulse width. Without the additional fiber picosecond pulses were not possible at rates in the megahertz regime.

With this general geometry the laser made it possible to observe multiple operating regimes with only minor changes to the cavity. The traditional method of harmonic

mode-locking provides interesting regimes depending on whether the modulator is driven at low harmonics ($1 \leq n < 100$) or very high harmonics ($n > 500$). Shifting the drive frequency off from a harmonic of the cavity by a predetermined amount allowed the laser to operate in a rationally mode-locked state producing pulses at rates as much as 10 times the applied frequency.

3.1.2 Mode-Locked Operation

The laser may operate in a number of different regimes producing different outputs. In all cases the output is taken from the output coupler and passed through another polarization controller and a polarization insensitive isolator. The isolator prevents any unwanted reflections from re-entering the laser cavity and subsequently altering the laser operation. The polarization controllers provide adequate adjustment of the polarization state to enhance second harmonic autocorrelation traces. In all regimes operational wavelength, power, repetition rates and pulse widths are collected and compared using the following diagnostic system.

A spectrum analyzer measured the operational wavelength of the laser; it had a resolution bandwidth of 0.1 nm allowing a facile means of monitoring the mode-locked operation by observing spectral broadening characteristics of mode-locking. When the laser output was cw, it's spectrum would mode hop from wavelength to wavelength with a linewidth limited by the resolution of the spectrometer. When the laser mode-locked, the spectrum settled on a single peak wavelength and the linewidth increased beyond the resolution limit indicating multiple modes had been successfully locked.

Initial operation of the ring laser was conducted at the fundamental cavity spacing which varied from 4.88 MHz $> \Delta\nu > 1.52$ MHz. These frequencies correspond to cavity lengths 41 m $< L < 136$ m. At these low repetition rates the drive frequency window for stable mode-locked operation is very narrow. Characteristics of a typical pulse at a frequency, $\Delta\nu = 1.519$ MHz are shown in Fig. (12). The pulse has a temporal profile best fit by a hyperbolic secant with a FWHM of 1.1 ps. The corresponding spectral width is 3.1 nm centered at 1561 nm. This width corresponds to a frequency bandwidth of 380 GHz. Assuming a hyperbolic secant shape, the time-bandwidth product of this pulse, $\tau\Delta\nu = 0.408$, exceeds the transform limited minima of 0.315. This value indicates additional pulse shortening might be achieved through better management of the cavity dispersion balanced by SPM. The output power of the laser was 5.9 mW which can provide the peak pulse power assuming a negligible background continuum via Eq. (36).

$$P_{peak} = P_{ave} \frac{T}{\tau_p} \tag{36}$$

The pulse shown in Fig. (12) has a peak power of 3.565 kW. The average pulse energy is 3.88 nJ.

It is important to note that pulse widths of this magnitude are much smaller than would be expected for an actively mode-locked erbium fiber laser. The calculated pulse width is approximately 500 ps. The actual pulse is two orders of magnitude shorter than the predicted width for purely active mode-locking implying that there is substantial nonlinear pulse shaping taking place. The high nonlinear effects are a result of the high

Figure 12: Output of the ring laser operating at the fundamental frequency. The temporal (a) and spectral (b) output from the fiber ring laser operating at the fundamental frequency, 1.519 MHz. The long cavity length provides sufficient anomolous dispersion to allow soliton pulse shaping as evidenced by the agreement between the observed pulse and a hyperbolic secant squared curve.

peak pulse power within the cavity. The internal peak power is four times the exiting pulse power, 14.26 kW, providing an intensity of 26.36 GW/cm^2 in Corning SMF-28 fiber with a core diameter of 8.3 μm. Although values vary for the nonlinear coefficient for fibers the earliest measured value for a silica glass fiber of 3.2 × 10^{-16} cm^2/W is still almost exclusively used.[24] The acquired phase shift for the peak of the pulse due to the nonlinear index of refraction is $\Delta\phi$ = 0.34 rad/cm, a very large value for a cavity with a length greater than 100 m. This nonlinear polarization rotation allows the linearly polarizing modulator to act as an intensity discriminator eliminating the less intense edges of the pulse.

The power spectrum of the pulse train could be analyzed using the theory proposed by von der Linde[1] to provide a measure of the timing-jitter. Fig. (13) shows the sharp peak and surrounding structure for the second and the tenth cavity harmonic to illustrate the differences between harmonics. To determine the nature of the noise, amplitude or temporal fluctuations, the dependence of the particular structure on the corresponding harmonic number must be determined. The sideband structures identified in Fig. (13) exhibited a low frequency noise component whose area followed an n^2 dependence, indicative of timing-jitter. Analyzing the higher harmonic spectra, the calculated timing-jitter of the pulse train proved to be 70 ps. This rather large timing jitter is a characteristic of passive rather than active mode-locking. Passive mode-locking dominates the pulse shaping since the effective transmission window of the modulator is much longer at low repetition rates when driven by a sinusoidal signal. This value could be improved by reducing that transmission window by using a pulse generator rather than a frequency synthesizer.
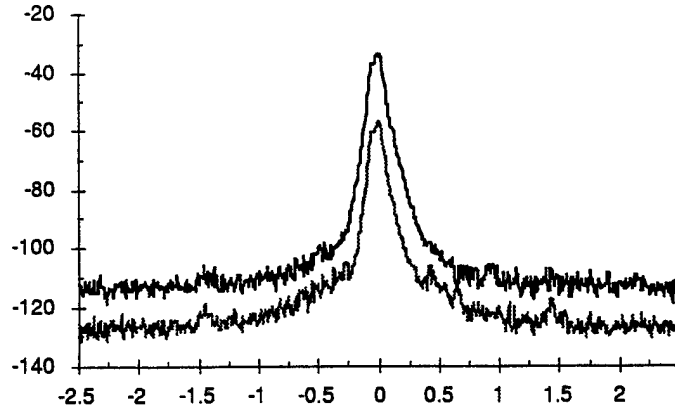
Figure 13: Power spectra of the ring laser operating at the fundamental frequency. Fourier components of the power spectrum of the ring laser operating at the fundamental cavity frequency. The spectra exhibit the characteristic rise in sideband noise and reduction of the peak powers as the harmonic number increases.

The ring laser can be operated at low repetition rates and still produce picosecond pulses. These pulse are not shaped by the action of the modulator as in pure active mode-locking, but by passive effects shaping the pulse within the cavity. The laser has the advantage of high output power but suffers from large timing-jitter. The jitter makes this system an unattractive choice for the synchronization experiments or applications which require a great deal of temporal stability.

When the laser was operated at much higher harmonics, generated by a synthesized signal generator. The cavity was shortened to have a fundamental cavity spacing of $\Delta \nu \sim 5$ MHz. The modulator was driven by a 5.006 GHz signal from the generator swinging a voltage of 1.24 V_{p-p}. This voltage translates to a modulation depth of 25% . Running at this frequency corresponds to laser operation at the 1024 harmonic. The predicted pulse width comes out to be on the order of 5 ps, which is in much closer agreement with the observed pulse widths, indicating that active mode-locking is the dominant pulse shaping mechanism.

The spectral and temporal profiles of the laser output are shown in Fig. (14). The observed pulse width of 7.13 ps and corresponding spectral width of 0.336 nm provide a time-bandwidth product of 0.296 which is slightly lower than the value of 0.315 for hyperbolic secant pulses. At this high repetition rate, the output power of the laser dropped to 0.6 mW. By again employing Eq. (36), the peak pulse power was calculated to be 16.8 mW. The high repetition rate significantly drops the peak power of the pulses decreasing the effectiveness of nonlinear pulse shaping within the cavity. This is evidenced by the wings present on the sides of the pulse. These wings mask the lower portions of the pulse where Gaussian and hyperbolic secant pulses diverge making it difficult to discern an accurate pulse shape.

The final measure of this systems operation was the noise analysis of the output. The low frequency noise sidebands observed in the power spectra again provided a measure
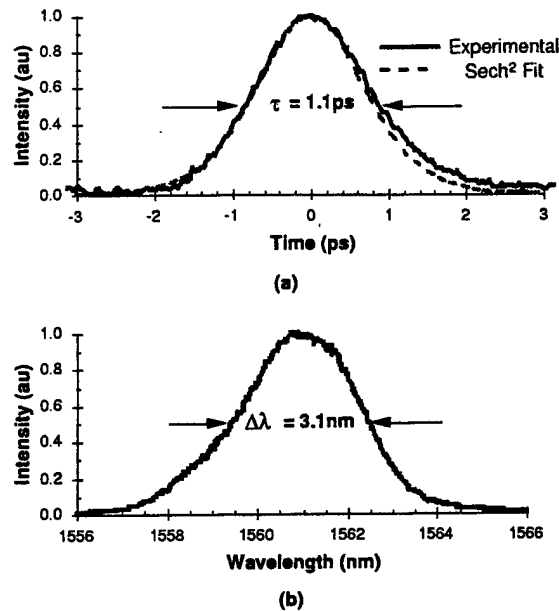
18
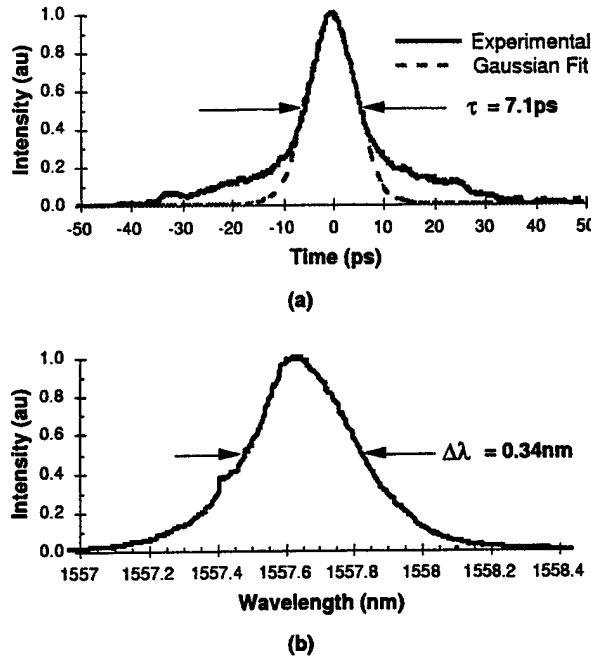
Figure 14: Output of the ring laser operating at the 1024th harmonic. The temporal (a) and spectral (b) output from the fiber ring laser operating at 5.006 GHz which corresponds to approximately the 1024 harmonic. The pedestal is due to insufficient nonlinear pulse shaping occuring within the cavity.

of the timing jitter of the pulses. Only four data points were available for measurement as the bandwidth of the spectrum analyzer extended only out to 21 GHz. The measured timing-jitter was approximately 1 ps which is significantly lower than the jitter observed at low repetition rates. The timing-jitter was most likely sub-picosecond, but because of the inability to examine harmonics higher than the fourth it could not be precisely determined. Since amplitude and timing fluctuations are comparable at the low harmonics, amplitude fluctuations could be contributing to the observed sideband energy.

The ability to operate at repetition rates above a gigahertz combined with low inherent timing jitter allows this laser to be used in a high speed communication architecture as a source or diagnostic tool for testing high speed photonic communication devices. A drawback to the present system is the low peak pulse power which typically requires significant amplification before the pulses can be effectively exploited in an application.

3.1.3 Rational Mode-Locking

Active mode-locking of a fiber ring laser routinely provides pulse trains at repetition rates in the gigahertz regime. Commercially available Mach-Zehnder $LiNbO_3$ modulators are capable of operating up to 18 GHz. State of the art modulators have been developed which allow operation at rates as high as 100 GHz, but even these are orders of magnitude beneath the carrying capacity of telecommunications fiber. To use as much of the available bandwidth as possible very elaborate WDM and TDM systems have been
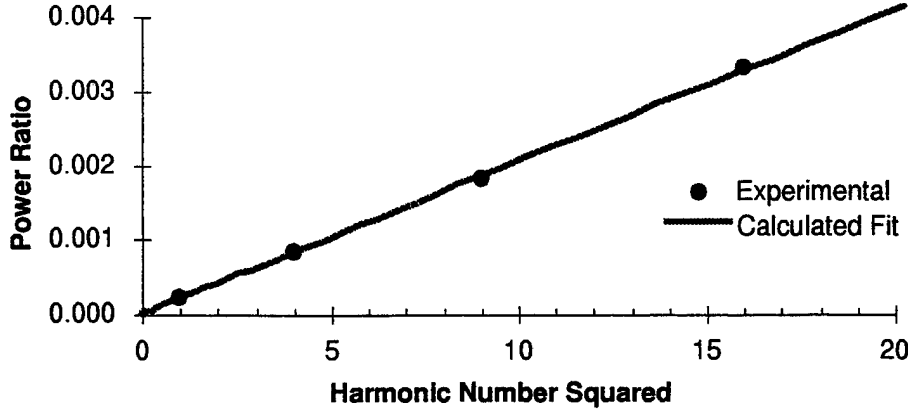
Figure 15: Power spectra of the ring laser operating at the 1024th harmonic. Plot of the ratio of the peak power levels of the delta and noise sidebands at the harmonic Fourier components of the pulse train. The ratio exhibits the n^2 dependence characteristic of timing jitter.

developed combining large numbers of pulsed laser sources operating at rates much lower than the final bit stream. The large number of expensive components to achieve these high rates makes these systems cost prohibitive. Rational mode-locking provides a means of achieving repetition rates as high as 200 GHz from a single laser source at the cost of lowering the output power.[22]

Rational mode-locking operates on the principal that pulsed operation can be achieved with the external signal not operating at a cavity harmonic, $f_{signal} \neq n\Delta\nu$, but rather when $f_{signal} = (n + \frac{1}{p})\Delta\nu$ where n and p are integers.[25] Driven by this signal the laser operates at repetition rates given by $f_{laser} = (np \pm 1)\Delta\nu$. The parameter p greatly increases the repetition rate with negligible demands placed on the modulator response. It will be shown that there is a limit to how large a value p can become before other effects hamper performance. Despite those limitations, this method provides a method of achieving very high repetition rates with components capable of only modest repetition rates.

Fig. (16) illustrates the propagation of a single pulse through the cavity. The pulse amplitude is attenuated by the partially transparent modulator producing the periodically varying pulse train. Within the cavity at any one time, there are $np \pm 1$ pulses providing an equivalent output pulse train. The modulator is completely transparent for only one of the pulses, however, and the subsequent pulses all suffer varying degrees of attenuation. The amount of attenuation depends on the relative position of the pulse relative to the pulse that passes through the modulator unattenuated.

The experiments relating to rational mode-locking were carried out with the ring laser having a fundamental cavity mode spacing of 1.52 MHz. The actual experiments were carried out by simply choosing a value for n and p and tuning the signal generator to the required frequency. Once the frequency was set, the output was viewed on an analog oscilloscope. In addition to the oscilloscope, the spectrum analyzer monitored the output for spectral broadening to ensure the laser remained mode-locked. Fig. (17) shows the
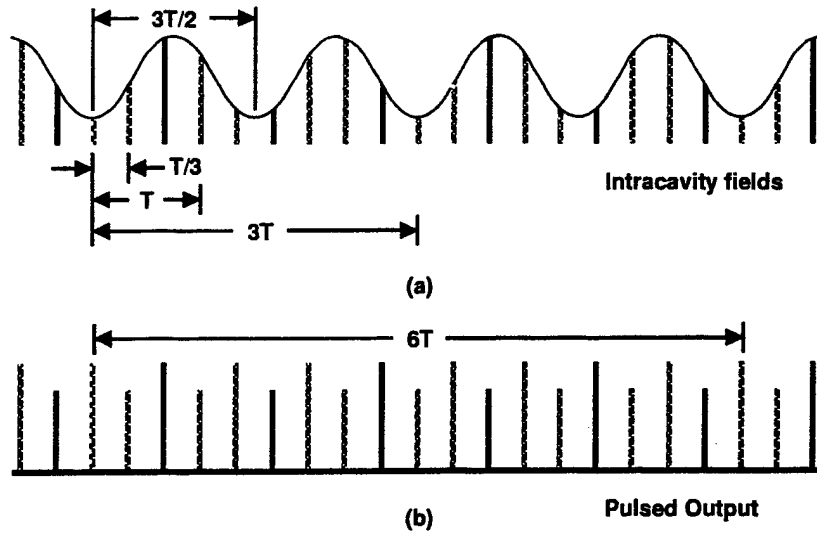
Figure 16: Rational mode-locking with $n = 1$ and $p = 2$. A graphical representation of the intracavity pulses (a) and the output pulse train (b) of a rationally mode-locked laser with $n = 1$ and $p = 2$. The intracavity pulses undergo an irregular modulation which is periodic in time with a period of $np + 1T$ or $3T$. The observed output is modulated with a period of pT or $2T$ which means the overall pulse series is periodic at $6T$.

operation of the laser with a drive frequency of only 1.82 MHz which corresponds to values of $n = 1$ and $p = 5$. At this drive frequency the laser operated at a repetition rate of 9.12 MHz. The modulator experienced a change in frequency of only 300 kHz or 19.7% while the repetition rate of the laser increased by a factor of 6. The increase in repetition rate comes with a cost in energy which can be seen in the resulting variations in pulse amplitudes due to the individual pulses experiencing unequal attenuation within the cavity. It is also interesting to note that as the drive frequency decreases, nearing the value of the actual harmonic frequency, the repetition rates dramatically increase.

As the value of p increases, two effects come to the forefront which limit or reduce the effectiveness of the mode-locking. The first is the attenuation due to the modulator. In every round-trip time a pulse is emitted which has experienced p trips around the cavity without the modulator being completely transparent. This effect is clearly visible in Fig. (18) where $n = 1$ and $p = 10$. The large envelope containing the pulses is characteristic of the sinusoidal drive signal applied to the modulator. The pulses nearest the transmission maxima experience little loss compared to those further away. This is an unavoidable affect observed even at the relatively low values of p as seen in Fig. (17).

The second problem which limits the maximum value p can assume is the competition between rational and harmonic mode-locking regimes. At large values of p the coupling between the modes falls very closely to the nearest neighbor as well as the mode $(np \pm 1)\Delta\nu$ away. As p increases the coupling between nearest neighbors takes over and the
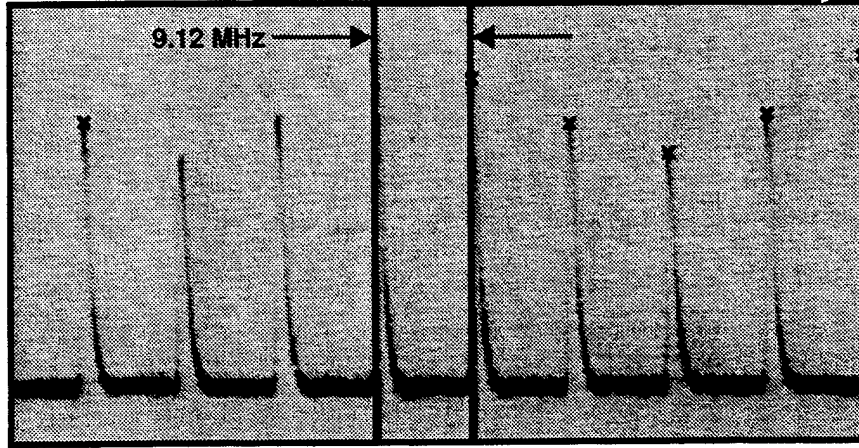
Figure 17: Rational mode-locking pulse train when $n = 1$ and $p = 5$. A rationally mode-locked pulse train with $n = 1$ and $p = 5$. The repetition rate which is six times the fundamental with the pulses appearing with a periodic modulation repeating every five pulses.

laser begins mode-locking at the harmonic frequency $n\Delta\nu$. To date the highest value of p which provided stable pulsed output is 16 by Jeon et al.[26]
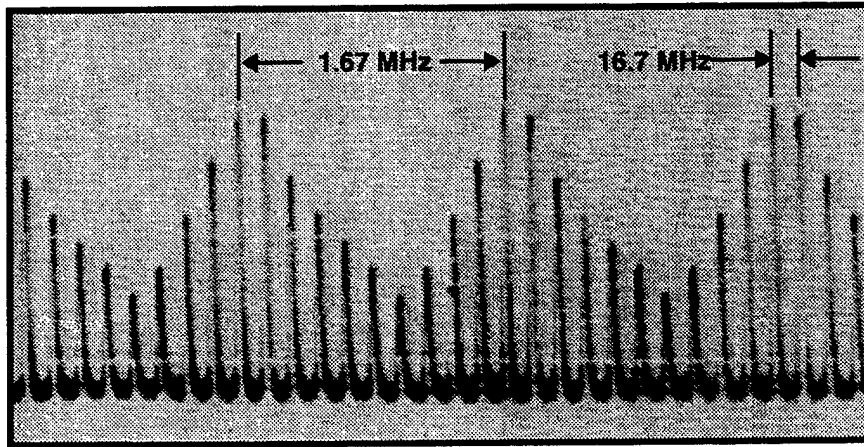
Figure 18: Rational mode-locking when $n = 1$ and $p = 10$ Rational mode-locking when $n = 1$ and $p = 10$. The pulse amplitudes are periodically attenuated with a frequency of 1.671 MHz which corresponds to the drive signal applied to the modulator.

3.2 Passively Mode-Locked Erbium Fiber Laser

Passively mode-locked fiber lasers which rely on the nonlinear effects of the fiber to generate sub-picosecond pulses via APM action have produced the shortest pulses from an erbium doped fiber attaining widths as narrow as 30 fs.[27] Lasers such as the figure eight and fiber ring are two common examples of the types of lasers which use APM, but these lasers are rarely self-starting and require ultrasensitive control of the polarization state

within the cavity. This sensitivity causes these lasers to suffer more from environmental fluctuations requiring delicate adjustment of the cavity birefringence to maintain optimal operation. These fluctuations have prevented passively mode-locked fiber lasers from finding widespread applications outside of the laboratory. Recent work has centered on the development of a compact, passively mode-locked fiber laser, which does not suffer from adverse birefringence effects.

The integration of semiconductor devices as bulk saturable absorbers into fiber lasers has proven to be an effective method for creating self-starting mode-locked fiber lasers.[28, 29] Loh *et al.* were the first to use a multiple quantum well saturable absorber as a nonlinear mirror in an integrated fiber Fabry-Perot fiber laser scheme.[30] This scheme had a distinct advantage over previously integrated fiber lasers in that it exhibited an immunity to changes in the cavity birefringence. This laser was capable of generating picosecond pulses with peak powers in excess of 30 W making this configuration an attractive choice as a compact picosecond pulse source.

This Section describes the construction and operation of a passively mode-locked erbium fiber laser employing a multiple quantum well saturable absorber. The optical properties of the saturable absorber will be described including a characterization of its reflection, linear and nonlinear absorption. The saturable absorber is then incorporated into various Fabry-Perot fiber laser configurations in an attempt to determine the optimal design of such a laser. It will be shown that this laser operates outside the soliton regime preventing effective nonlinear pulse shaping due to the fiber. In these lasers the cavity loss is the predominant variable in determining the shape and width of the output pulse.

3.2.1 Optical Characterization of the MQW Saturable Absorber

The saturable absorber used in these experiments was formed by thin semiconductor layers which when alternately stacked upon one another form one-dimensional quantum wells. These wells are capable of absorbing radiation in the near infra-red region producing the desired optical modulation. The quantum wells were comprised of alternating layers of 10 nm $In_{0.53}Ga_{0.47}As$ wells and 10 nm $In_{0.52}Al_{0.48}As$ barriers. The sample was comprised of 50 periods of wells and barriers. The quantum wells were grown directly on a semi-insulating InP substrate with a thickness of approximately 500 μm. The quantum well region encompassed a total thickness of only 1 μm. This sample differed from other nonlinear mirrors in that the ètalon effects as a result of the total thickness were a concern. A distributed Bragg reflector grown under the MQW region would eliminate these effects and has been shown to work effectively in many fiber lasers employing a MQW nonlinear mirror.[30] A time resolved pump-probe experiment using 100 fs pulses from a mode-locked Cr^{4+}:YAG laser[31] measured the relaxation time of the MQW sample to be approximately 271 ps. The long relaxation time puts the mode-locking action out of the fast saturable absorber regime so the shaping mechanisms should assume slow saturable absorber dynamics. The samples from Dr. Gary Wicks of The Institute of Optics at the University of Rochester, Rochester, NY, were grown by molecular beam epitaxy . The experiments which characterized the optical properties of the MQW saturable absorber were carried out by Dr. Mike Hayduk of Rome Laboratory, Rome, NY.[32]

  i. **Reflectance**

An important aspect of integrating semiconductor devices into optical systems is the large differences in the index of refraction at the air/semiconductor interfaces. These differences result in large, unwanted reflections which make reliable measurements of the optical properties of these devices a non-trivial matter. In all cases both in the characterization and application of these MQW saturable absorbers the light was directed to the sample at normal incidence. This greatly simplifies the calculation of the reflection losses due to the air/semiconductor interfaces.

The index of refraction for the $In_{0.52}Al_{0.48}As$ barrier on top of the MQW is 3.24.[33] This value gives a top surface reflectance of $r_1 = 0.28$. The index for the InP substrate is listed as 3.1[34] and provides a reflectance of $r_2 = 0.26$.

The sample is then treated as a Fabry-Perot ètalon to calculate the respective reflected intensity of the MQW mirror. The reflectivity is sensitively dependent on the wavelength and cavity thickness. Fig. (19) illustrates the dependence of the reflectivity on wavelength. The massive fluctuations are a result of the long cavity length relative to the wavelength. The effect is enhanced by the large index, $n = 3.1$, of the substrate. A small change in the cavity length of only 0.5 μm will effect a phase shift of 2π.
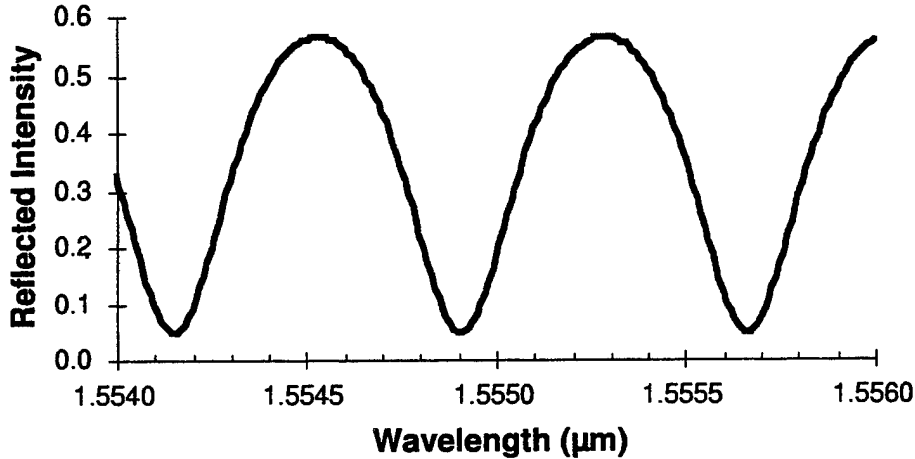
Figure 19: Reflectivity of the saturable absorber. The reflectivity of the saturable absorber at the wavelengths of laser operation. The drastic changes in reflectivity are due predominantly to the thickness of the InP substrate.

ii. Linear Absorbance

The linear absorbance was measured using a monochrometer and a white light source. The white light source was focused onto the sample and then focused onto an 0.275 meter triple grating spectrometer. The light was then collected and passed to a transimpedance amplifier. The signal was measured using a lock-in amplifier and passed to a computer where the resulting transmission data could be recorded.

A baseline measurement was recorded prior to the sample to provide a measure of the intensity of the spectral components of the white-light source. The transmission from the sample was then recorded as the monochrometer varied the wavelength. The baseline and transmission curve are combined to provide the linear absorbance according to Beer's

law.

$$I(L) = I(0)\exp\left\{-\int_0^L \alpha(\mathbf{r})\mathrm{d}l\right\} \tag{37}$$

where $I(0)$ and $I(L)$ are the incident and transmitted intensities respectively, and L is the thickness of the of the MQW region. The substrate has negligible absorption in the 1.5 μm region where the measurements were made. The relative interface reflectances cause some difficulties when calculating the MQW absorbance. The baseline transmission must be scaled to account for the reflections at the front and back semiconductor/air interface. Ètalon effects which could cause a standing wave to build up in the sample were neglected. The linear absorbance for the sample used in these experiments is shown in Fig. (20).
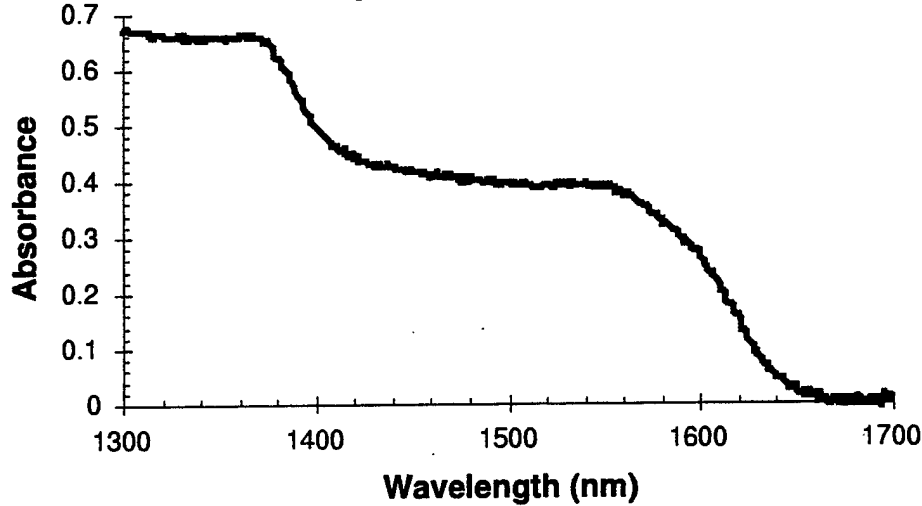
Figure 20: Linear absorbance of the saturable absorber. The linear absorbance of the saturable absorber. The laser operated in the 1550 to 1560 nm region near the top of the lower shoulder in the curve.

iii. Nonlinear Transmission

Using a tunable cw Cr^{4+}:YAG laser capable of emitting 400 mW of power at 1550 nm, the nonlinear or intensity dependent transmission of the MQW saturable absorber was measured.[31] The laser output was passed through a 3 dB fiber coupler with one output connected to a Newport 818 IR detector and the other directed at the MQW sample. The resulting transmission through the sample was recorded and compared to the incident power exiting the other arm of the coupler. Care was again taken to account for the surface reflections of the MQW sample. Incident intensities ranging from 0.1 - 20 kW/cm^2 were used, but complete bleaching of the sample was not observed as shown in Fig. (21). The fitted curve was calculated to determine the saturation intensity for the sample.

The relation between the incident and transmitted intensity for a saturable absorber may be expressed as:

$$\ln\frac{I(L)}{I(0)} - \frac{I(0) - I(L)}{I_{sat}} = -\alpha L \tag{38}$$

Eq. (38) has is a transcendental equation for the transmission $T = I(L)/I(0)$, which is numerically determined. The values of the normalized absorbance was calculated to be
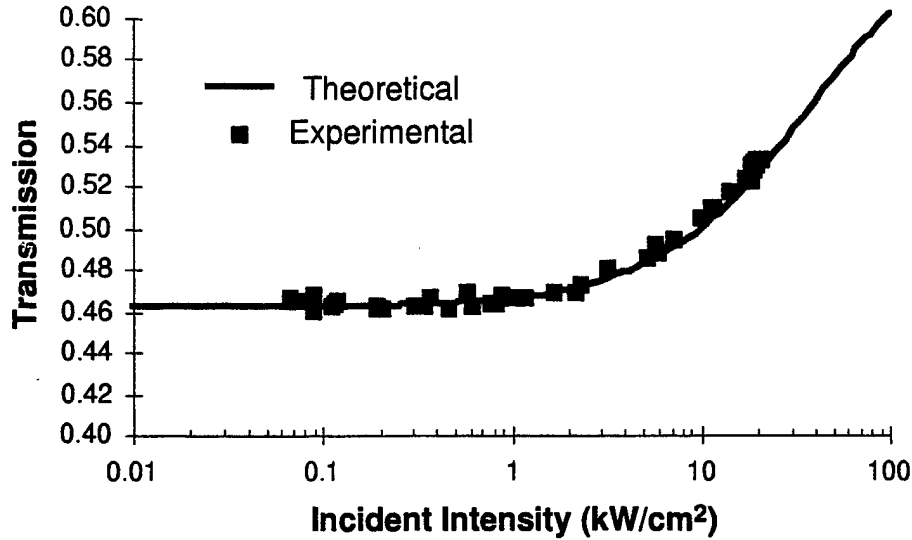
Figure 21: Nonlinear transmission of the saturable absorber. Intensity dependent transmission of the saturable absorber. The saturation intensity was measured at 1.27 kW/cm² with no observed flattening of the transmission due to insufficient incident intensities.

0.34 while the saturation intensity was 1.27 kW/cm² at 1550 nm. This value for the saturation intensity is easily accessible at modest intra-cavity powers for a fiber laser when one considers the very small beam size inside a fiber, approximately 50 μm².

3.2.2 Laser Operation with a Free Space Coupling Interface

The MQW laser is comprised of three sections common to a laser in a Fabry-Perot configuration. The layout of the laser in this initial setup is shown below in Fig. (22). The gain was provided by a 2.5 m length of erbium fiber provided by the group at NRL. The erbium was pumped by a fiber pigtailed laser diode which puts out approximately 80 mW at 980 nm. The pump was introduced to the cavity through a fiber Bragg grating which acted as the output coupler of the cavity. The power measurements were made after the pump light had passed through the grating and therefore provide an accurate measure of the power reaching the erbium fiber.
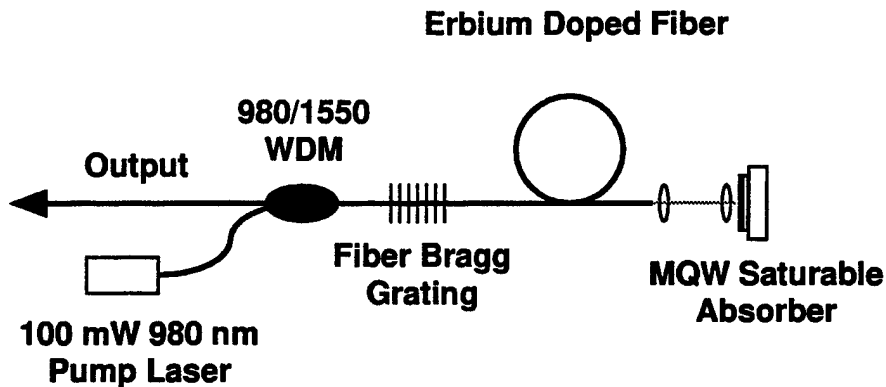
Figure 22: MQW laser cavity using free space focusing. Schematic showing the layout of the MQW laser with the light focused onto the nonlinear mirror.

The fiber Bragg grating had a peak reflectance of 49% centered at 1556 nm. The grating exhibited a reflection bandwidth of 1.0 nm at FWHM. This grating allows the pump light to pass unattenuated while reflecting the desired operating wavelength. The simplicity of the design eliminates the need for any free space bulk optics and shortens the cavity by allowing the WDM and any couplers to be placed outside the laser resonator. There are drawbacks to employing this fiber Bragg grating as the output mirror of the cavity, however.

The grating reflects only a very narrow band acting as a spectral filter as well as an output coupler. This filtering prevents the laser from operating at its preferred wavelength and reduces efficiency which is normally determined by the gain and loss dynamics of the cavity as a whole. The grating also limits the spectral bandwidth of the laser to 1.0 nm at FWHM. This restriction places limits on the narrowest pulse widths which can be obtained. Operating at 1556 nm and assuming a Gaussian pulse shape, the narrowest obtainable pulse would have a duration of approximately 3.5 ps. The pulses are not presently limited by the grating, but it could prove to be a limitation in future configurations.

An additional length of undoped fiber was spliced onto the end of the erbium increasing the cavity length to approximately 6.7 m giving a fundamental cavity frequency of 14.89 MHz. The fiber allowed the end of the fiber cavity to be cleaved without removing portions of the gain medium.
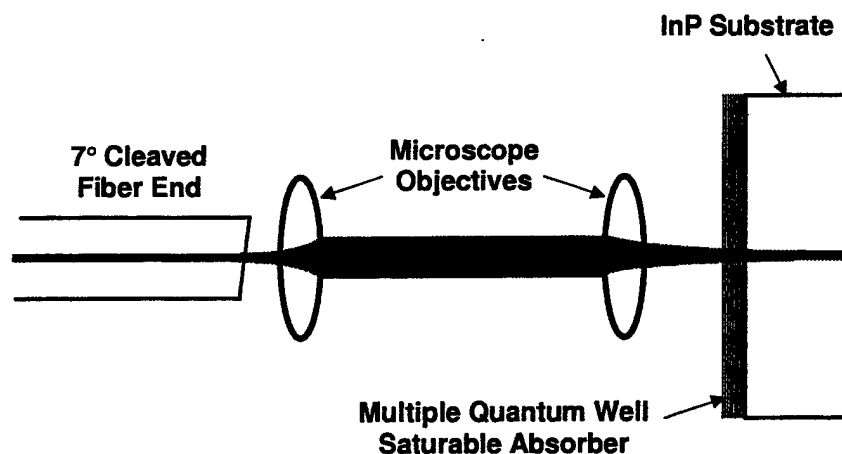
Figure 23: Free space coupling between the fiber cavity and nonlinear mirror. An enlarged schematic of the focusing of the intracavity light onto the nonlinear mirror. Using the microscope objectives, the optimal coupling back into fiber was calculated to be 30%.

The nonlinear mirror was introduced into the cavity using two microscope objectives acting both as collimating and focusing lenses. The coupling of this setup has an optimal feedback efficiency of approximately 30%. The setup shown in Fig. (23) allows the adjustments to be made along the face of the nonlinear mirror as well as the depth of focus. The focusing of the light on the MQW saturable absorber dictated the local intensity at the mirror which in turn determines the depth of modulation provided by the absorber. The actual beam diameter inside the saturable absorber could be altered by

nonlinear effects such as self-focusing occurring within the absorber. The output power varied with the lateral position of MQW mirror and had a maximum output power of 6 mW.

Mode-locked operation is induced by bringing the MQW mirror into the focus of the beam exiting the second lens shown in Fig. (23). Stable operation depends critically on the location of the beam relative to the mirror surface. Inhomogeneities caused during the growth of the sample require the beam to find a particular region of the mirror. The spectral response of the MQW mirror varies due to ètalon effects which prevent stable cw mode-locked operation. Once the system begins cw mode-locked operation the system is stable against minor perturbations to the system. The laser can be turned off and will immediately begin mode-locking when restarted.
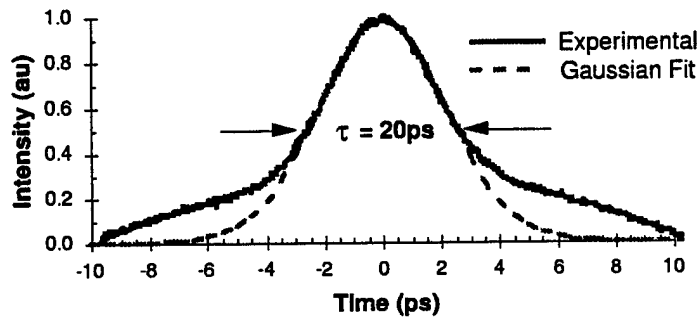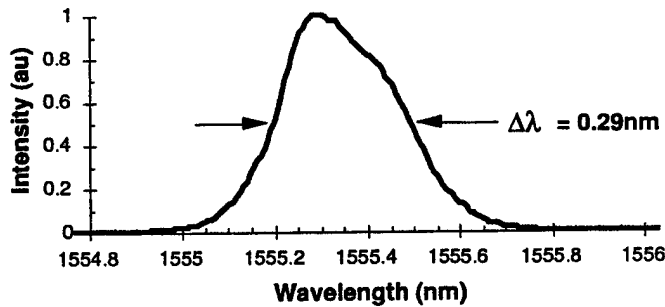
Figure 24: Output of the MQW laser using free space focusing. The temporal (a) and spectral (b) output from the MQW laser using the free space focusing.

The laser produced 20 ps pulses with a Gaussian profile. The corresponding spectral width was 0.29 nm centered at 1555.3 nm. These values provide a time-bandwidth product of 0.7301 which is much larger than the Fourier limited value of 0.4415. A characteristic autocorrelation trace and the corresponding spectrum are shown in Fig. (24). The wings on the edges of the pulse trace again mask the actual pulse shape, but a Gaussian pulse is fitted to the top of the curve to illustrate how greatly the two diverge. The asymmetry in the wings of this pulse were a result of inconsistencies in the autocorrelators stepper motor. The laser suffered from periodic amplitude fluctuations of as much as 10% at frequencies of approximately 300 kHz. These amplitude fluctuations appear in the power spectrum as noise spikes symmetrically located about the sharp spikes at harmonics of the laser cavity. These amplitude fluctuations or relaxation oscillation

result from cavity gain/loss dynamics.

(a)

(b)
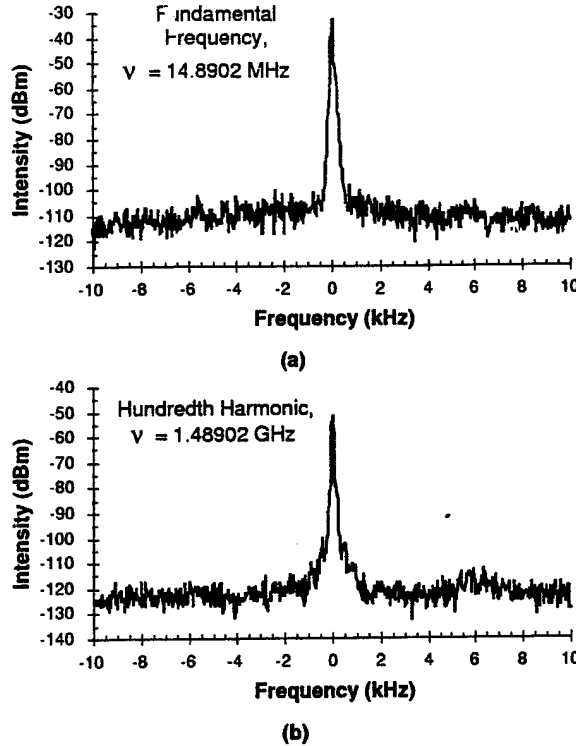
Figure 25: Power spectra of the MQW laser with free space focusing. Power spectra at the fundamental (a) and hundredth (b) harmonic of the MQW laser operating with the free space focusing. The hundredth harmonic shown in (b) has a distinct sidebands at its base as opposed to the fundamental frequency shown in (a). These sidebands are characteristic of timing jitter.

The noise of this laser appeared to be dictated by stationary process characteristic of an actively mode-locked laser rather than the non-stationary processes predicted by passively mode-locked lasers.[35] This behavior was characteristic of the MQW laser regardless of the configuration. sharp spikes surrounded by the noise sidebands are clearly visible in Fig. (25). Examining the low frequency sidebands surrounding the center peaks at harmonics of the power spectrum showed the predicted n^2 behavior for timing-jitter. The lower harmonics exhibited a higher peak power than expected indicating the presence of amplitude fluctuations in the low frequency sidebands. Only at the lower harmonics was this visible as the effects of the amplitude noise drops of relative to the timing-jitter at higher harmonics. The laser exhibited timing jitter ΔT less than 1 ps, which is exceptionally small for a passively mode-locked fiber laser. The reduced timing jitter was due to the presence of the grating as will be shown in the next section.

3.2.3 Laser Operation with a High Reflective Mirror

In an effort to reduce the loss in the cavity, the fiber Bragg grating was replaced with a broad band high reflector dielectric mirror. The mirror, $R_{max} > 99\%$ at 1550 nm, was butt-coupled to a flat cleaved fiber end. The two were brought into contact to eliminate

29

unwanted ètaloning effects from occurring between the two surfaces. The redesigned cavity is shown in Fig. (26). The mirror was highly transmissive at the pump wavelength of 980 nm which permitted any unabsorbed pump intensity to pass out of the cavity.
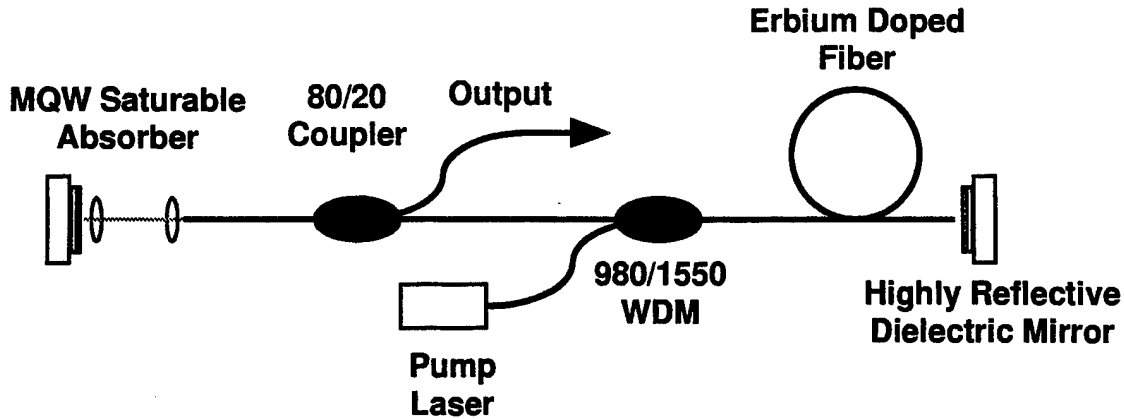
Figure 26: MQW laser configuration with the dielectric mirror. Schematic of the MQW laser with a dielectric mirror in place of the fiber Bragg grating. The dielectric mirror provided a broader reflective bandwidth which allowed the laser to determine its preferred operational wavelength.

The absence of the fiber Bragg grating requires the cavity be lengthened to include the WDM and an output coupler within the laser resonator itself. The output coupler was a 80/20 fiber coupler placed just before the MQW mirror as shown in Fig. (26). The presence of the coupler and WDM did little to alter the operation of the cavity other than to introduce additional anomalous dispersion. This setup reduced output loss to around 1 dB as opposed to 3 dB with the fiber Bragg grating.

The broad reflectivity of the mirror allows the laser to select the wavelength of operation rather than the narrow reflectivity of the fiber Bragg grating which in this case increased to 1559.8 nm as shown in Fig. (27) (b). The spectrum broadened but did not broaden significantly in the absence of the fiber Bragg grating which was capable of supporting the displayed bandwidth of 0.452 nm at FWHM. The pulse widths are slightly narrower than the previous case with the observed width being 7.2 ps. The pulse has a temporal profile closely resembling that of a hyperbolic secant rather than the Gaussian profile in the earlier configuration. This shape is indicative of soliton-like pulse shaping occurring within the cavity which was earlier prevented by the very large loss of the cavity. The pulses were not transform limited as the time-bandwidth product was 0.40 which is greater than the Fourier limited product of 0.3148. These pulses also possessed a very large pedestal with a width as large as 2 ns which could be observed in oscilloscope traces taken with a 20 GHz sampling head as shown in Fig. (28). The background pedestal results from the competing mechanisms of soliton pulse shaping and mode-locking due directly to the saturable absorber. No adjustment of the MQW mirror eliminated these background pedestals from the pulse train.

The power spectrum of this laser was similar in appearance to that observed in the previous configuration. The spectral sidebands due to the timing-jitter had increased
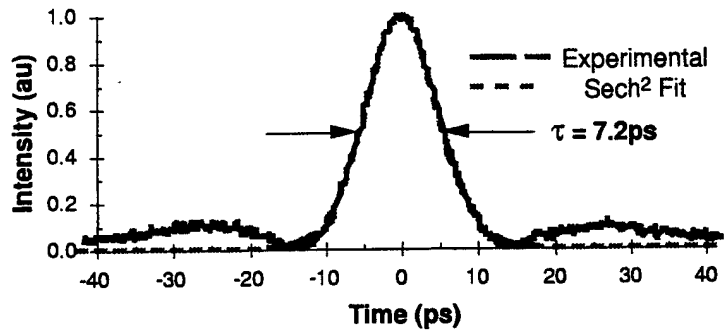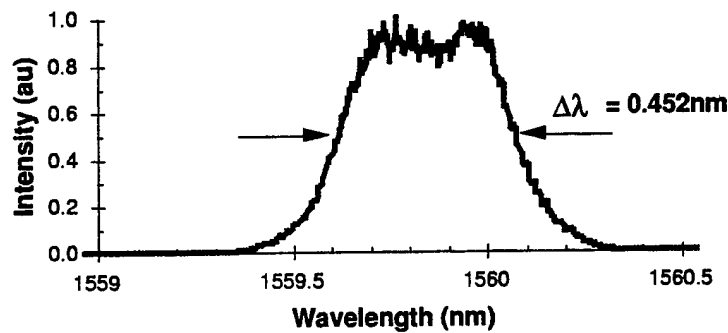
Figure 27: Output from the MQW laser with the dielectric mirror. The temporal (a) and spectral (b) output from the MQW laser using the dielectric mirror. The temporal profile is well approximated by a hyberbolic secant squared fit which is indicative of 'soliton' shaping occurring within the cavity.

by an order of magnitude so the calculated timing jitter became $\Delta T > 65$ ps. This increase resulted from the reduction of the loss in the cavity due to the presence of the dielectric mirror rather than the grating. The reduced loss in the cavity would permit greater correlation of the pulses allowing the accumulated timing jitter to increase. In the presence of excessive loss the pulses would operate in a more independent manner with the temporal position more a result of the cavity length rather than the relative position of the previous pulse. The presence of the large pedestal could also account for the increased timing-jitter. Given the long duration of the pedestal these timing fluctuations could be a result of their fluctuations which would mask the actual jitter of the smaller pulses. As the narrower pulses ride on the large pedestal, any timing-jitter experienced by the pedestal would also be observed in the narrow pulses as well.

3.3 Laser Operation with Fiber Butt-Coupled to MQW Mirror

The laser was initially operated in a configuration which brought the fiber end directly butt-coupled to the MQW mirror. The fiber was cleaved and brought up to the MQW sample using a XYZ stage. We were unable to determine the exact distance from the sample to the fiber end however a measurement using a high reflective dielectric mirror
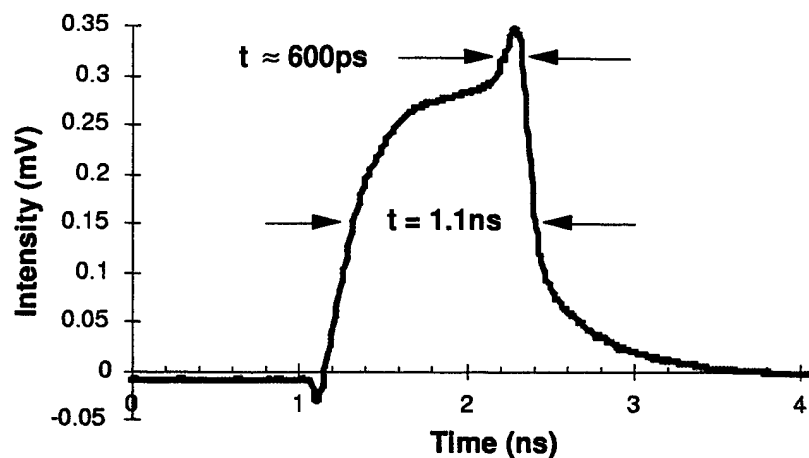
Figure 28: Oscilloscope trace exhibiting the large background pedestal. An oscilloscope trace of the output which exhibits a large background pedestal when the dielectric mirror is present.

indicated that the coupling efficiency dropped by 3 dB at a distance of 10 μm. A microscope was used to monitor the relative distance between the sample and the fiber to prevent unwanted contact between the two.
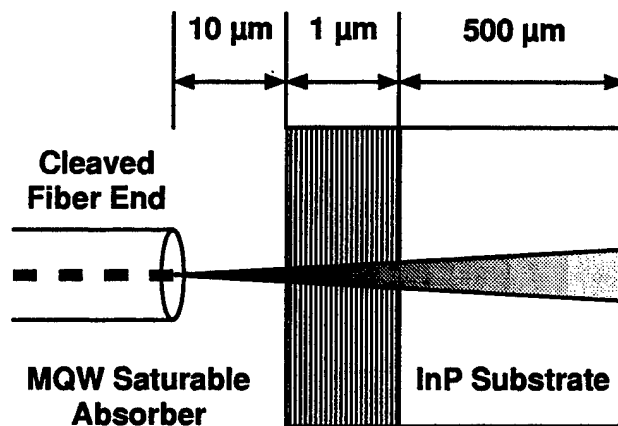
Figure 29: Butt-coupling between the fiber and the MQW saturable absorber. An enlarged schematic of the fiber-nonlinear mirror interface. This method was extremely simple to use as it required no additional bulk optics but suffered from increased coupling losses. The nominal coupling efficiency for this scheme was approximately 1.5%.

The interface is shown in Fig. (29) and allows us to approximate the coupling of the light back into the fiber. The analysis follows the work done by Dietrich Marcuse in calculating the coupling of light from one fiber to another.[36] The light exiting the fiber has a Gaussian intensity profile and a beam waist of approximately 5 μm. The beam diverges after exiting the fiber at an angle of 7.6° assuming an NA of 0.13 of standard SMF-28 silica fiber. The beam continues to diverge through the sample, reflects off the back surface and reenters the fiber. This analysis neglects any nonlinear effects such as absorption and possible self-focusing which could occur within the sample. Using an

overlap integral to calculate the reflected radiation coupled into the fiber, the coupling coefficient, T, becomes

$$T = \frac{4(4Z^2 + 1)}{(4Z^2 + 2)^2 + 4Z^2} \tag{39}$$

where Z is the normalized fiber separation distance which is defined as

$$Z = \frac{D\lambda}{2\pi n w^2} \tag{40}$$

where D is the twice the distance of the fiber end to the back of the saturable absorber, n is the index of refraction of the fiber and w is the mode-field radius of the Gaussian beam in the fiber. Using values typical of SMF-28 fiber and a separation between the fiber end and the back of the sample of 511 μm, the calculated coupling efficiency is $T = 0.021$. Using the maximum reflected value the coupling efficiency for this is less than 1.5%

$$\eta = T \times R = 0.0135 \tag{41}$$

This poor coupling efficiency in addition to the high loss of the fiber Bragg grating acting as the output coupler provide a resonator with an incredibly low finesse of 0.25. This high loss prevents soliton like pulses from evolving within the cavity, and pulse shaping due to the saturable absorber is also reduced due to the low coupling efficiency.
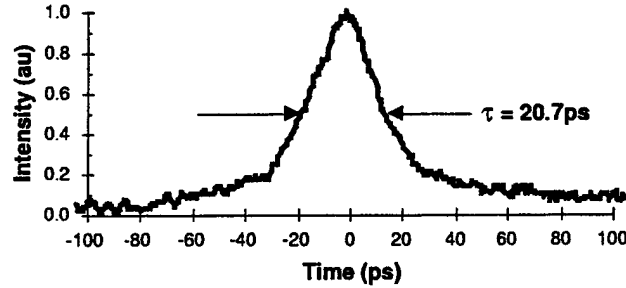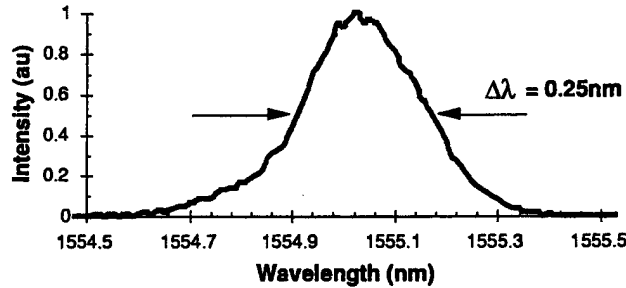
Figure 30: Output of the MQW laser with nonlinear mirror butt-coupled. The temporal (a) and spectral (b) output from the MQW laser using the butt-coupled interface between the fiber and nonlinear mirror. The temporal profile is very noisy, a result of the large cavity losses in this setup.

The pulsed output from this laser is shown in Fig. (30). The pulses exhibit an optical spectral shape similar to other configurations employing the fiber Bragg grating with a

spectral width of 0.23-0.36 nm. The pulses have a temporal width which varied with the location of the fiber on the MQW mirror. Observed pulses varied in width from 7 to 30 ps, but the temporal profile was never well approximated by either hyperbolic secant nor Gaussian. The pulses again exhibit a very large pedestal and suffer from large amplitude fluctuations. The amplitude fluctuations again occurred at periodic intervals due to relaxation oscillations within the cavity. The period of these fluctuations varied from 10 - 100 μs. The large amplitude noise dominated the power spectrum preventing an effective measurement of the timing jitter from being made.

4 Synchronized Mode-Locked Erbium Fiber Lasers

4.1 Introduction

There are new methods of mode-locking being developed to take advantage of the more desirable properties of passively and actively mode-locked lasers. These hybrid mode-locked lasers attempt to achieve the narrow pulse widths and high pulse energies while retaining the low noise and controllable repetition rate of actively mode-locked lasers. In addition to improving laser performance, hybrid mode-locking via synchronization with an external source is a very important enabling technology for key time-domain applications including high speed optical clock recovery. Numerous methods exist for constructing these hybrid lasers. Some combine an actively mode-locked laser with a passive pulse shaping cavity directly attached[37] while others drive a passively-mode locked laser with the output from an actively mode-locked.[38, 39] This Section concerns itself with the latter laser type as these are most commonly associated with laser synchronization.

Temporal synchronization is a means of inducing a laser to operate at a repetition rate which is identical to some external frequency source illustrated in Fig. (31). A simple example is active mode-locking which synchronizes a frequency synthesizer and the optical pulse stream in time. Synchronization in a hybrid mode-locked laser implies a locking of the output from the synchronized or slave laser to another optical pulse stream, the master signal. The synchronized output can then be used in conjunction with the master signal to realize many potential optical devices such as high speed optical signal processing. For example, high-speed time-domain networks require that a local laser be locked to an incoming data stream to within a bit period, which can be as short as a few picoseconds. The local laser must be synchronized to the data stream within that bit period to avoid unacceptable error rates.

We focus here on injection-locking of the MQW laser to obtain temporal synchronization, a hybrid mode-locked state. Passively mode-locked lasers rely on nonlinear effects within the cavity to lock the modes of the cavity. The master signal acts as a perturbation to the nonlinear elements of the slave laser causing it to pulse at the same rate as the perturbation. Some methods typically used in fiber lasers to obtain hybrid mode-locking via injection locking include loss[40], multimode[41] and most commonly cross-phase modulation.[42, 43]. The system presented here relied on loss modulation of the MQW saturable absorber by an incoming stream of high intensity pulses.
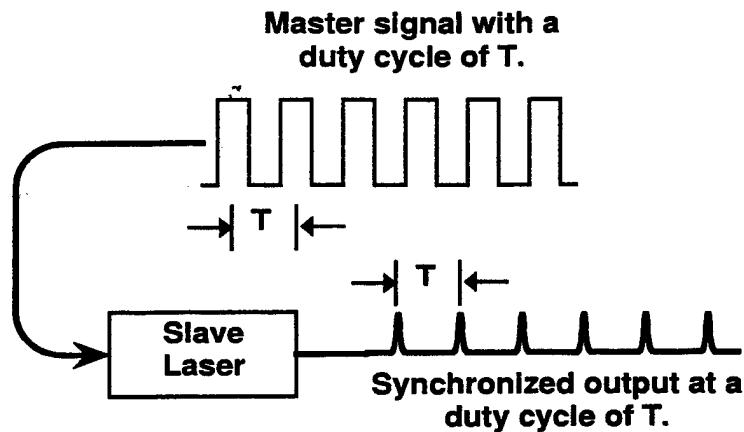
**Master signal with a
duty cycle of T.**

Figure 31: Temporal synchronization induced by injection of an external signal.

4.2 Experimental Configuration

Injection-locking of a passively mode-locked fiber laser necessarily requires the generation of a pulse stream to act as the master signal. The master signal was produced by the actively mode-locked laser, and was used to synchronize the output from the MQW modelocked fiber laser. The general layout of the synchronization scheme is shown in Fig. (32).

A 3dB coupler placed before the WDM of the slave laser injected a portion of the master signal while the slaved output was taken out through the remaining port. The coupler reduces the power entering the slave laser by half reducing the effectiveness of the modulation. To compensate for the loss in power an erbium fiber amplifier was constructed. The amplifier was comprised of 15 m of ATT EDF-HE980 erbium doped fiber pumped by approximately 90 mW of 980 nm light. The master laser put out an average power of 1.35 mW which increased to 20.6 mW after passing through the amplifier providing 11.8 dB of gain. Not all of the power found its way into the pulses as a strong increase in the background fluorescence was observed. The amplifier allowed the master signal to achieve power levels high enough to effectively modulate the saturable absorber. The master signal enters the slave laser through the fiber Bragg grating. Provided there is no spectral overlap between the master pulses and the reflection band of the grating, the pulses will enter the cavity unattenuated. Adjustments to the polarization controller in the master laser could sufficiently separate the two spectra.

The output of the MQW laser was directed to a fast photodetector where it could be observed on an oscilloscope. The oscilloscope was triggered off of the signal generator driving the ring laser. Only when the two lasers were temporally synchronized could the MQW laser output be observed stably on the oscilloscope. In some cases the observed pulses would simply be the amplified re-emission of the master signal. Passing through the MQW cavity, the master signal experiences gain passing through the erbium fiber reducing that available for the MQW laser. In these cases there would be no observable emission on the optical spectrum analyzer within the gain band of the fiber Bragg grating. Only when the spectrum was present and exhibiting spectral broadening along with a stable pulse train on the oscilloscope could the lasers be said to be synchronized.
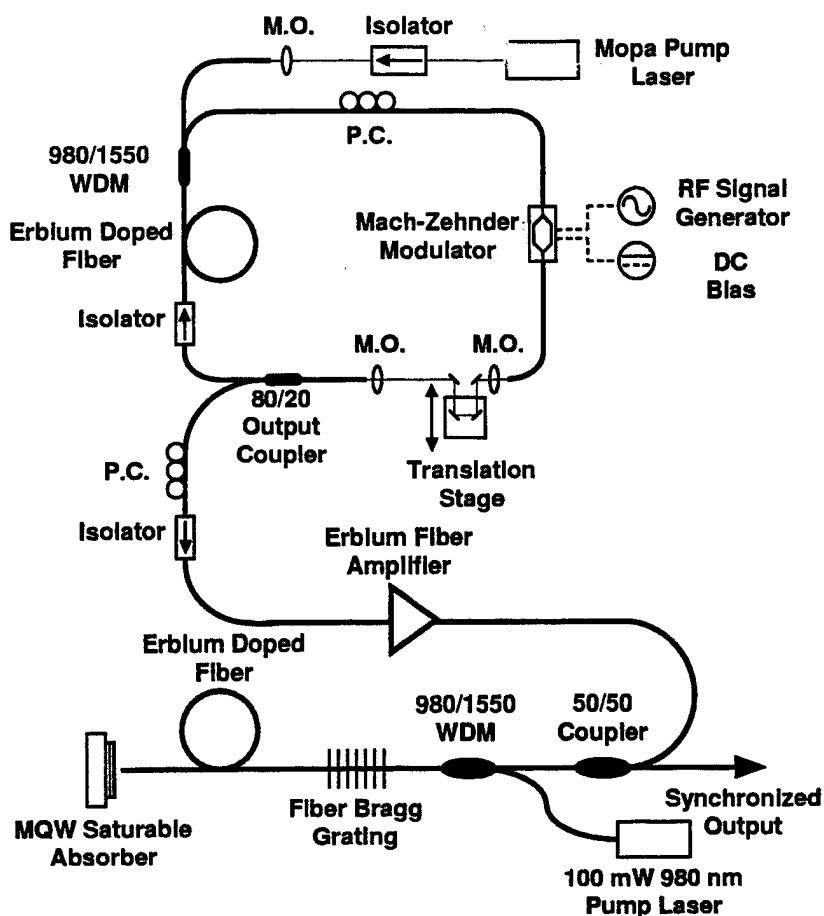
Figure 32: Configuration of the synchronization scheme.

4.3 Synchronization at the Fundamental Frequency

The MQW laser operated at a repetition rate of 3.5435 MHz and the cavity of the ring laser was increased to match. The ring laser was made to operate at a frequency of 3.5435 ± 100 Hz at a wavelength of 1558 nm. The pulses were approximately 3 ps in duration with a spectral width of 1.5 nm at FWHM. At this wavelength the master signal could enter the MQW laser through the fiber Bragg grating. The lasers began synchronized operation at the fundamental frequency of 3.5435 MHz as observed on an oscilloscope in Fig. (33). The threshold injection power was determined to be approximately 1.5 mW which corresponds to a peak pulse power of 140 W and a pulse energy of 400 pJ.

The slave laser was able to put out pulse widths which varied from 9 to 30 ps in a fashion similar to that observed when operated in an independent mode-locked state. The pulse width depended critically on the position of the fiber to the MQW mirror rather than the power of the master signal. This seems to indicate that the master signal serves only to control the timing of the MQW laser cavity and there is no additional modulation due to the master signal within the resonator. Spectrally the MQW laser output contained both the master and slave signal as observed in Fig. (34). The peak output from the master signal is more than 10 dBm below that of the MQW laser ensuring that the observed phenomena is indeed synchronization and not amplified reemission of the master signal.
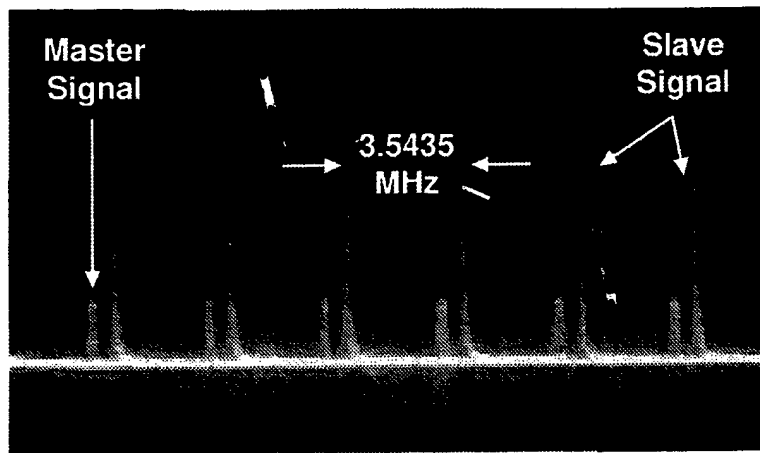
Figure 33: Synchronized output from the master and slave laser

The ring cavity was detuned from the operating frequency of 3.5435 MHz to determine the range of frequencies over which synchronization would occur. The lasers demonstrated synchronization over a frequency range from 3.54385 MHz to 3.5432 MHz providing an effective fractional bandwidth of 1.83×10^{-4}. As the detuning increased it became necessary to inject more power as the synchronization threshold increased. The furthest detuning limits required injection powers in excess of 5 mW.

The actual intensities needed to effectively modulate the absorber could not be precisely determined since the master signal interacts with the erbium fiber before striking the saturable absorber. The erbium fiber of the laser cavity acts as an amplifier increasing the intensity of the master signal. Couplers were impractical to avoid the master signal passing through the gain as the proportional power the coupler lets into the cavity it will also emit on the return pass. With a lossy resonator to begin with additional losses were unacceptable to maintain mode-locked operation. Large injection powers necessitate that the ring laser be limited to operation at very low repetition rates which exhibit very large timing jitter. Because of this it was not possible to observe any timing jitter reduction in the synchronized output due to injection locking.

Synchronization was also independent of the polarization state of the master signal which could prove to be a useful trait for possible clock recovery schemes. Long distance pulse transmission suffers from polarization mode dispersion (PMD) or the randomizing of the polarization state in transit. Clock recovery methods which require strict control of the polarization state suffer and in some cases may be impractical. These semiconductor devices are indifferent to the polarization state and thus not subject to PMD limitations.

4.4 Synchronization at the Second Harmonic

The butt-coupled configuration proved to be unable to support synchronized operation at harmonics of the laser cavity. The system was then redesigned to include the free-space optics to reduce the losses within the cavity and the cavity length was reduced to operate at a repetition rate of 20 MHz. The ring cavity was likewise redesigned to operate at approximately 5 MHz. At this rate the laser would need to be run at its fourth harmonic
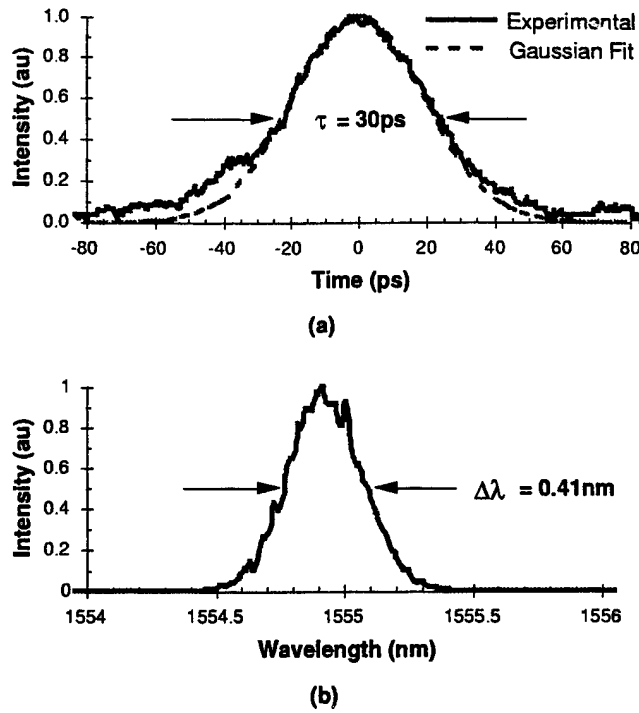
Figure 34: Synchronized output at the fundamental cavity frequency. The temporal (a) and spectral (b) output from the MQW laser when synchronized to the fiber ring laser. The pulse again exhibits a gaussian envelope.

reducing the available power per pulse by a quarter; however, the cavity required the additional span of fiber to obtain sufficient nonlinear polarization rotation to maintain short stable mode-locked output. Approximately 9 mW of power was injected into the laser cavity providing a comparable peak power and pulse energy per pulse as in the case with the MQW mirror butt-coupled to the cavity. With a 3 ps pulse the peak power was approximately 150 W with a pulse energy of 450 pJ.

With the maximum intensity of the master signal injected into the cavity, the MQW laser was induced to operate at the second harmonic of the cavity fundamental repetition rate. The signal was insufficient to lock the laser output to the master signal with the pulses intermittently synching and then slipping into independent operation at the second harmonic. This indicates that the laser can in fact operate at higher harmonics, but the required perturbation to the saturable absorber is still too high for effective synchronization at these rates. The output from the MQW laser running at its second harmonic is shown in Fig. (35) exhibiting the spectral broadening at the MQW laser's operating wavelength characteristic of mode-locking. An examination of the power spectrum of the MQW laser showed a reduction of power at the fundamental cavity frequency of more than 20 dBm relative to the sharp peak observed in the spectrum at the operating repetition rate of approximately 40 MHz. This reduction, shown in Fig. (36), confirmed that the laser was indeed operating at the second harmonic. Since the laser was operating in an independently mode-locked state the power spectrum was similar to those acquired with the laser running in this configuration at the fundamental frequency.

Attempts to operate the laser at higher harmonics was not possible as the injection intensities were unable to sufficiently perturb the saturable absorber. The high loss in the cavity also meant that a large portion of the energy needed to support multiple pulses within the cavity was being lost at the mirrors. Reduction of loss by the incorporation of

38
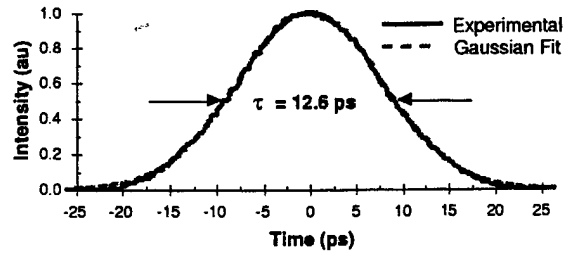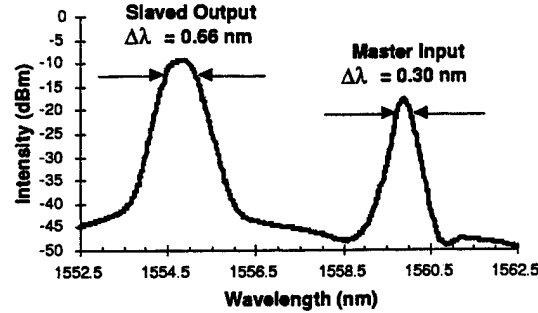
Figure 35: Output of the MQW laser operating at the second harmonic. The temporal (a) and spectral (b) output from the MQW laser .when induced to operate at its second harmonic. The respective spectra from the MQW (slave) and fiber ring (master) lasers can be clearly seen in (b).

a distributed Bragg reflector beneath the MQW stack and a Bragg grating with a higher reflectivity would greatly increase the available energy for multiple pulses. The highest rates sustainable would be limited by the recovery time of the saturable absorber which in this case is 270 ps. This value puts the system well within the realm of high speed optical communication where a 2 GHz signal has a 500 ps pulse separation.

5 Summary

The theory of mode-locked lasers was developed with parameters and conditions that are gleened from our understanding of the laser physics. We examined the action of a slow saturable absorber and nonlinear refraction on the mode-locked operation. We were particularly aware that the experimental conditions were more appropriate for a laser that was far outside the soliton-shaping regime. In this case we had to develop a different theoretical approach, based on nonlinear dynamics theory, to accurately solve the complex Ginzburg-Landau equation and its extensions. We were able to identify several new operating regimes and especially we found conditions under which apparently stable pulses were formed. For parameter ranges that are comaprable to the experimental conditions, the theoretical pulse widths are generally within a factor of two or three of the experimental results. This has encouraged us to look for further into the models and search for possible causes of the disagreement. We are continuing that endeavor.

Operation of an actively mode-locked erbium fiber laser was demonstrated in three operating regimes. The laser was capable of producing picosecond pulses at repetition rates ranging from 1 MHz - 5 GHz with output powers on the order of 1 mW. Observed pulse widths were shorter than those predicted by simple active mode-locking theory indicating additional soliton shaping was occurring within the cavity. The cavity disper-
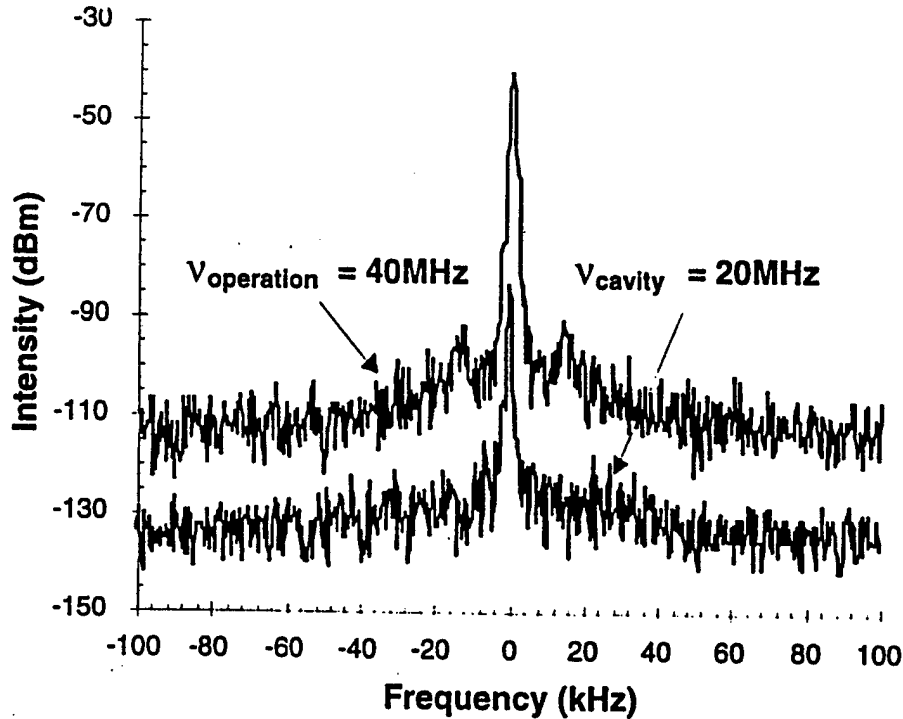
Figure 36: Power spectra of the MQW laser operating at the second harmonic. Power spectra of the MQW laser output at both the fundamental and second harmonic frequencies. The peak at the fundamental cavity frequency has been suppressed by more than 20 dBm from the operating frequency of 40 MHz indicating the laser is indeed operating above the fundamental frequency.

sion was not optimized for the pulse energies since the pulses were not transform-limited hyperbolic-secant pulses.

Rational harmonic mode-locking was demonstrated as a means to achieve higher repetition rates than the bandwidth of the modulator. These higher rates come at the cost of additional cavity loss and unequal pulse amplitudes. It has been demonstrated that the unequal amplitudes can be removed by circulating the pulses in an external cavity which is a sub-harmonic of the pulse repetition rate.

The laser provides a suitable source for a number of applications, most notably those relating to optical fiber communications. Examination of this laser operating in a synchronized system will be provided later. This synchronized system could be further expanded to model a true clock-recovery system crucial to any high speed communication systems. The wavelength tunability, variable repetition rates and narrow pulse width are important factors which make actively mode-locked fiber ring lasers attractive sources for communication applications.

A multiple quantum well saturable absorber was integrated into a Fabry-Perot fiber laser cavity creating a self-starting cw passively mode-locked laser. The inordinately high cavity loss prevents strong soliton pulse shaping and induces large periodic amplitude fluctuations. Reductions in cavity loss by improving the feedback from the nonlinear mirror in addition to reduced output coupling have indicated that it is possible to get some

40

soliton shaping further shortening the pulses. Further reduction in loss would require improvements made to the multiple quantum well saturable absorber with the possible inclusion of a highly reflective distributed Bragg reflector grown under the quantum wells. A summary of the observed operation of the MQW laser in all three configurations is provided in Table (1).

Table 1: Summary of the output of the MQW laser.

Laser Configuration

	Focused spot with Bragg grating	Focused spot with dielectric mirror	Butt-coupled with Bragg grating
Pulse Width (ps)	20	7.2	7-30
Spectral Width (nm)	0.2	0.45	0.25-0.35
Time-Bandwidth Product	0.73	0.40	0.5
Timing-Jitter (ps)	<1	70	–
Pulse Shape	Gaussian	Sech^2	–

The noise of the lasers varied with the particular configuration. The combination of the free space focusing on the nonlinear mirror combined with the fiber Bragg grating produced picosecond pulses with timing-jitter only 10% of the pulse width. Further reduction in the loss with a highly reflective mirror replacing the grating resulted in narrower pulses more closely with a pulse shape best approximated by a hyperbolic secant. These pulses appeared on a large background pedestal which resulted in a ten-fold increase in the timing-jitter, possibly an effect of the broad pedestal. Large cavity losses were incurred when the grating was returned to the cavity and the nonlinear mirror was butt-coupled to the fiber cavity. The subsequent large amplitude fluctuations prevented an accurate measure of the timing-jitter of this laser.

The free space coupled laser exhibited properties which makes it an attractive source for short pulse applications. A limiting trait of this and other passively mode-locked fiber lasers are the relatively long repetition times resulting from the long cavity lengths. Fiber lasers of similar design with shorter cavities have exhibited output repetition rates as high as 2.5 GHz producing soliton pulses which suffer from high timing-jitter.

It was demonstrated that the MQW laser could be effectively synchronized at the fundamental cavity frequency by the introduction of an external optical signal into the

cavity. The injected signal modulates the loss of the saturable absorber which causes the MQW laser to pulse synchronously with the modulation. When compared to the output of the MQW laser running independently, the synchronized output is indistinguishable. The synchronized state is stable over a detuning range of 1.83×10^{-4} fractional bandwidth and unaffected by changes to the polarization state of the injected signal.

By increasing the repetition rate of the injected pulses, the MQW laser could be induced to operate at a rate twice that of independent operation. The perturbation was sufficient to start operation at this rate but unable to maintain synchronization. The inability to operate at higher repetition rates was due to a combination of insufficient energy in the cavity and low intensity injection pulses. The output of the hybrid laser operating in both the synchronized state and independently at the second harmonic is summarized in Table. (2).

Table 2: Summary of the output of the hybrid laser.

	Repetition Rate	
	---	---
	Fundamental	Second Harmonic
Pulse Width (ps)	10-30	7.2
Spectral Width (nm)	0.30-0.40	0.45
Synchronized	Yes	No

The synchronization scheme described in this report has the potential to become a viable technology for high speed optical clock recovery. The two most attractive features for this application are the wide synchronization window and immunity to PMD. By permitting the injection signal to occupy any region of the absorber band edge except for that occupied by the Bragg grating, this laser is ideally suited to a massive WDM system. Different channels occupy different wavelength regions and this laser could be synchronized to any channel that doesn't reflect off the grating. Long distance transmission introduces a random polarization state on the data stream which makes synchronization schemes which require strict control of the polarization state impractical. Since the synchronization of the MQW laser is strictly intensity dependent, PMD effects are not important. Improvements which allow the laser to realize the gigahertz rates permitted by the relaxation time of the absorber are the first step toward realizing an actual clock recovery system.

References

[1] D. von der Linde, "Characterization of the Noise in Continuously Operating Mode-locked Lasers," Appl. Phys. B **39**, 201-217 (1986).

[2] H. A. Haus and A. Mecozzi, "Noise of Mode-locked Lasers," IEEE J. Quant. Electron. **29**, 983-996 (1993); M. Margalit, M. Orenstein and H. A. Haus, "Noise in Pulsed Injection Locking of a Passively Modelocked Laser," IEEE J. Quant. Electron. **32**, 796-801 (1996).

[3] I.N.Duling,III and M.L.Dennis, *Compact Sources of Ultrashort Pulses*, Cambridge Univ. Press, 1995.

[4] S.Tsuda, W.H.Knox, S.T.Cundiff, W.Y.Jan, and J.E.Cunningham, IEEE J.Quant.Electr.**2**, 454 (1997)
B.C.Collings, K.Bergman, and W.H.Knox, Optics Letters **22**, 1098 (1997)

[5] I.D.Jung, F.X.Kartner, L.R.Brovelli, M.Kamp, and U.Keller, *Opt.Lett.*, **20**, 1892 (1995).

[6] B.C.Barnett, L.Rahman, M.N.Islam, Y.C.Chen, P.Brattacharya, W.Riha, K.V.Reddy, A.T.Howe, K.A.Stair, H.Iwasmura, S.R.Friberg, and T.Mukai, *Opt.Lett.*, **20**, 471 (1995).

[7] M.Hayduk, *Ph.D.Thesis*, Cornell University, 1997.

[8] W.Kaechele, J.W.Haus, M.Hayduk, R.Erdmann, and K.Teegarden, Proc.SPIE-Int.Soc.Opt.Eng. **3075**, 16 (1997)
W.Kaechele, Ph.D.Thesis, Rensselaer Polytechnic Institute, 1997.

[9] H.A.Haus, J.G.Fujimoto, and, E.P.Ippen, J.Opt.Soc.Am. B **8**, 2068 (1991)
H.A.Haus, in *Compact Sources of Ultrashort Pulses*, ed. by I.N.Duling,III and M.L.Dennis, Cambridge Univ. Press, 1995.

[10] F.X.Kartner, I.D.Jung, and U.Keller, IEEE J.Quant.Electr. **2**, 540 (1996)

[11] J.M.Soto-Crespo, N.N.Akhmediev, and V.V.Avanasjev, J.Opt.Soc.Am. B**13**, 1439 (1996).

[12] A.C.Newell and J.A.Whitehead, J.Fluid Mech. **38**, 279 (1969).

[13] W.van Sarloos and P.Hohenberg, Physica D**56**, 303 (1992)
W.van Sarloos, Phys.Rev. A**37**, 211, (1988), A**39**, 6367 (1989).

[14] J.A.Powell, A.C.Newell, and C.K.R.T.Jones, Phys.Rev. A**44**, 3636 (1991)
C.K.R.T.Jones, T.M.Kapitula, and J.A.Powell, Proc.R.Soc.Edinburg A**116**, 193 (1990).

[15] G. Shaulov, I. Gabitov and J. W. Haus, "Pulse and Front Propagation in Optical Cavities,", in preparation (1998).

[16] J. D. Kafka, T. Baer and D. W. Hall, Opt. Lett. **14**, 1269 (1989).

[17] J. K. Smith, J. R. Armitage, R. Wyatt, N. J. Doran and S. M. J. Kelly, Electron. Lett. **26**, 1149 (1990).

[18] H. Takara, S. Kawanishi, M. Saruwatari and K. Noguchi, Electron. Lett. **28**, 2095 (1992).

[19] X. Shan, D. Cleland and A. Ellis, Electron. Lett. **28**, 107 (1992).

[20] G. T. Harvey and L. F. Mollenauer, Opt. Lett. **18**, 107 (1993).

[21] T. Pfeiffer and G. Veith, Electron. Lett. **29**, 1849 (1993).

[22] E. Yoshida and M. Nakazawa, Electron. Lett. **32**, 1370 (1996).

[23] R. P. Davey, K. Smith and A. McGuire, Electron. Lett. **28**, 482 (1992).

[24] R. H. Stolen and C. Lin, Phys. Rev. A **17**, 1448 (1978).

[25] N. Onodera, A. J. Lowery, L. Zhai, Z. Ahmed and R. S. Tucker, Appl. Phys. Lett. **62**, 1329 (1993).

[26] M. Y. Jeon, et al., Optical Society of America Annual Meeting, Lon Beach, CA, paper TuNN3, 1997.

[27] D. J. Richardson, A. B. Grudinen and D. N. Payne, Electron. Lett. **28**, 778 (1992).

[28] M. Zirngibl, L. W. Stutz, J. Stone, J. Hugi, D. DiGiovanni and P. B. Hansen, Electron. Lett. **27**, 1734 (1991).

[29] E. A. DeSouza, et al., Electron. Lett. **29**, 447 (1993).

[30] W. H. Loh, et al., IEEE Photon. Tech. Lett. **5**, 35 (1993).

[31] M. J. Hayduk, S. T. Johns, M. F. Krol, C. R. Pollack and R. P. Leavitt, Opt. Comm. **137**, 55 (1997).

[32] M. J. Hayduk, Doctoral Thesis, Cornell University (1997).

[33] S. Nojima and H. Asahi, J. Appl. Phys. **63**, 479 (1988).

[34] M. Shur, Physics of Semiconductor Devices (prentice-Hall, Englewood Cliffs, NJ, 1990).

[35] D. Eliyahu, R. A. Salvadore and A. Yariv, J. Opt. Soc. Amer. B **14**, 167 (1997).

[36] D. Marcuse, Bell Sys. Tech. J. **56**, 703 (1977).

[37] T. F. Carruthers, I. N. Duling and M. L. Dennis, Electron. Lett. **30**, 1057 (1994).

[38] B. K. Mathason and P. J. Delfyett, Proc. of SPIE **3075**, 52 (1997).

[39] L. E. Adams, E. S. Kintser and J. G. Fujimoto, Electron. Lett. **30**, 1696 (1994).

[40] W. Kaechele, et al., Proc. of SPIE **3075**, 16 (1997).

[41] M. Margalit, M. Orenstein and G. Eisenstein, Opt. Lett. **20**, 1877 (1995).

[42] K. Smith and J. K. Lucek, Electron. Lett. **28**, 1814 (1992).

[43] M. Obro, P. Thorsen and S. B. Andreasen, Electron. Lett. **30**, 1243 (1994).